Science Advances
AAAS

Supplementary Materials for

Real-space imaging of nanoparticle transport and interaction dynamics by graphene liquid cell TEM

Sungsu Kang, Ji-Hyun Kim, Minyoung Lee, Ji Woong Yu, Joodeok Kim, Dohun Kang, Hayeon Baek, Yuna Bae, Byung Hyo Kim, Seulki Kang, Sangdeok Shim, So-Jung Park, Won Bo Lee, Taeghwan Hyeon, Jaeyoung Sung*, Jungwon Park*

*Corresponding author. Email: jungwonpark@snu.ac.kr (J.P.); jaeyoung@cau.ac.kr (J.S.)

Published 3 December 2021, *Sci. Adv.* **7**, eabi5419 (2021)
DOI: 10.1126/sciadv.abi5419

The PDF file includes:

Other Supplementary Material for this manuscript includes the following:

S1. Estimation of the vertical dimension of graphene liquid cell

A. Thickness measurement by low-loss electron energy loss spectroscopy

The thicknesses of a liquid encapsulated within a graphene liquid cell (GLC) can be measured using electron energy loss (EEL) spectroscopy and the log-ratio method (*24*).

$$\frac{t}{\lambda} = \ln\left(\frac{I_t}{I_0}\right) \tag{S1-1}$$

where t is the thickness of the sample, λ is the inelastic mean free path of electron, I_t is the total number of electrons in the spectrum, and I_0 is the number of electrons which have lost no energy. To extract the contribution of the graphene windows from $t_{total}/\lambda_{total}$ of the GLC, the thickness of the liquid could be calculated as follows (*25*):

$$t_{water} = \left(\frac{t_{total}}{\lambda_{total}} - 2\frac{t_{graphene}}{\lambda_{graphene}}\right)\lambda_{water} \tag{S1-2}$$

Here, $2t_{graphene}/\lambda_{graphene}$ can be measured from a dry, graphene-only region near a GLC in which two sheets of few-layer graphene overlaps. The inelastic mean free path of electrons at 200 keV in water, λ_{water}, is estimated to be 320 nm (*26*).

In order to measure the thickness of the liquid in a GLC with Eq. (S1-2), the location of the GLC was first found in TEM mode, and EEL spectroscopy is performed in the same location in STEM mode. An annular dark-field STEM image showing the GLC and the nearby dry region is shown in Fig. 1B, and averaged EEL spectra obtained from those regions are shown in Fig. 1C. As a result, $t_{total}/\lambda_{total}$ and $2t_{graphene}/\lambda_{graphene}$ is respectively obtained to be 0.28 and 0.25 with Eq. (S1-1), yielding the liquid thickness of ~9.6 nm.

Above calculation relies on the assumption that the encapsulated liquid is pure water. Since the exact concentrations of the other components cannot be measured precisely, the

calculation is repeated by assuming that the GLC is filled only by NaCl. The electron inelastic mean free path at 200 keV in NaCl is given by 229 nm (*27*). The resulting thickness in the case of NaCl filling is ~6.9 nm. It is likely that the actual thickness of the encapsulated liquid would lie between two values (6.9 ~ 9.6 nm), obtained from the pure water and the pure NaCl in the GLC. This estimation for the liquid thickness made by EELS is consistent with results obtained from the geometrical analysis and the image simulations of GLC (see below).

B. Thickness measurement by geometrical relationship in morphology of GLC

The height of the liquid pocket can also be estimated using the geometrical scaling relationship between the height and the lateral size established for a bubble encased between a graphene monolayer and a substrate (*28*). When the encapsulated bubbles are smaller than approximately 500 nm, they tend to be round with the height-to-radius ratio being approximately 0.1. For bubbles whose sizes are larger than 500 nm, they usually have triangular or trapezoidal shapes. We captured an image that shows shape and size of the liquid pocket containing nanoparticles recorded in movie S1 (Fig. S6). The liquid pocket shows a round shape with a radius of approximately 50 nm so that it can be classified as a round-type bubble according to ref. (*28*). Considering the GLC is composed of two graphene sheets, the height of the liquid pocket can be estimated to be about 10 nm with height-to-radius ratio, 0.1, and the radius, 50 nm, of the liquid pocket.

C. Observation of transient overlaps between nanoparticles

The thickness of the encapsulated liquid can be confirmed from the time-series TEM images showing overlaps between nanoparticles. We identified an event in which images of three nanoparticles stay overlapped for a few seconds without coalescence between them (Fig. S7). Each

of the three nanoparticles can be identified in the time-series TEM images as the overlapped regions between them are darker than other regions. In addition, each of the nanoparticles initially overlapped by the others can be distinguished later as they diffuse away from the other nanoparticles. Therefore, the encapsulated liquid is expected to be thicker than the three nanoparticles arranged side by side along the viewing direction of the TEM with a little gap between them. Considering that the measured diameters of the three nanoparticles are given by 1.4 nm, 1.4 nm, and 1.7 nm, and the length of ligand molecules on the nanoparticle surfaces is 0.7 nm, the thickness of the confined liquid is larger than at least 8.7 nm, which is the sum of the effective diameters of the three ligand-passivated nanoparticles.

D. Comparison to simulated TEM images of GLC

The estimated thickness of the GLC is further confirmed by comparing TEM images generated from model GLCs with known thicknesses and the experimental TEM images. At first, we performed molecular dynamics simulations for model GLCs consisting of TIP3P water molecules (*29*) between two sheets of graphene with the Large-scale Atomic/Molecular Massively Parallel Simulator (LAMMPS) package (18 Jun 2019 version) (*30*). The lateral dimensions of the simulation box were set to 82.38 Å by 82.38 Å. The simulation was performed multiple times by changing the height of the simulation box (the distance between two graphene sheets) from 4 nm to 12 nm with a step size of 2 nm. The top frozen graphene sheet was rotated in-plane by 11 degrees with respect to the bottom frozen graphene sheet to reproduce the bihexagonal pattern observed in the fast Fourier transform (FFT) of a TEM image in our experiment (see Fig. S8). The number of TIP3P water molecules varies with the height of the simulation box to match the density of water to 1 g/cm^3. A CHARMM force field was implemented to simulate TIP3P water molecules under

300 K and 1 bar. After an energy minimization and 100 fs-long NVT ensemble simulation with a time step of 1 fs and the Nosé-Hoover thermostat, we performed the NPT ensemble simulation with the Nosé-Hoover barostat for 100 ps.

The TEM simulations of the model GLCs were performed using the multislice algorithm (*31*). The simulation boxes were split into 1 Å-thick slices parallel to the graphene sheets. Acceleration voltage, third-order spherical aberration, fifth-order spherical aberration of microscope, absolute temperature, and the number of phonon configurations were set to 200 kV, 1 mm, 3 mm, 300 K, and 5, respectively. Varying values of defocus were used, explicitly, 0, -50, -100, and -150 nm. The standard deviation and the sampling size for the defocus distribution were set to 40 Å and 10 Å, respectively. The size of an objective aperature was set to 30 mrad with values of the minimum illumination angle and the maximum illumination angle being given by 0 mrad and 1 mrad, respectively. Finally, Gaussian noise with a signal-to-noise ratio of 0.9 was added to make the simulated TEM images resemble experimental images. The FFTs of the resulting TEM images was performed using bulit-in scripts embedded in MATLAB.

The hexagonal patterns, characteristic of hexagonal periodicity of a graphene, shown in the FFT of the simulated TEM images can be detected only if the thickness of the GLC is sufficiently thin, usually smaller than 10 nm (Fig. S9). Due to the randomly placed water molecules between the graphene sheets, the hexagonal FFT patterns become blurred and disappear as the thickness of the water layer increases. The maximum thickness beyond which the hexagonal pattern is not detectable was found to be 10 nm, which is in good agreement with our estimation of GLC thickness calculated using the geometrical relationship between the vertical and the lateral dimensions of the GLC.

S2. Calibration of nanoparticle trajectories

TEM observation performed at high magnifications often suffers from uncontrolled movement of a specimen stage, known as drift. The TEM specimen stage drift will hinder correct interpretations of nanoparticle dynamics unless properly managed. Based on the assumption that nanoparticles in the GLC do not show directional bias, mean nanoparticle velocity can be used to obtain drift-free nanoparticle trajectories. Here, the mean nanoparticle velocity, $\langle v_\alpha(t)\rangle$ ($\alpha \in \{x, y\}$), in the α-direction is calculated by averaging instantaneous velocities, $\{v_\alpha^i(t)\}$, of individual nanoparticles in the α-direction (Figs. S10A and S10B, lines). The noisy profile of $\langle v_\alpha(t)\rangle$ was subsequently smoothened by an FFT filter using built-in scripts embedded in MATLAB (Figs. S10A and S10B, bold lines). The low-pass filtered mean velocities, $\langle v_\alpha(t)\rangle_f$, reflect the overall directionality of nanoparticles, which can be attributed to the movement of the TEM specimen stage. Finally, we calibrated nanoparticle trajectories with $\langle v_\alpha(t)\rangle_f$ as follows: $x_a^i(t) = x_b^i(t) - \int_0^t dt' \langle v_x(t')\rangle_f$ and $y_a^i(t) = y_b^i(t) - \int_0^t dt' \langle v_y(t')\rangle_f$, where $(x_b^i(t), y_b^i(t))$ and $(x_a^i(t), y_a^i(t))$ respectively denote the two-dimensional coordinates of the *i*th nanoparticle at time *t* before and after calibration. The low-pass filtered mean velocities calculated after calibration are vanishingly small at any time *t* (Figs. S10C and S10D).

The validity of the drift correction procedure described above was confirmed based on the *in situ* TEM movie of immobile nanoparticles dried on a substrate. The specimen was prepared by placing a drop of gold nanoparticle solution on a graphene-coated TEM grid and drying overnight. JEOL JEM-ARM200F TEM equipped with Gatan OneView detector installed at National Center for Inter-University Research Facility (NCIRF) was used to observe the nanoparticles on the graphene substrate. Due to the drift of the TEM specimen stage, all nanoparticles observed within

the field of view appear to move in one direction (Fig. S11A), and the mean nanoparticle velocities have non-zero values during the observation (Fig. S11C and S11D, lines). The low-pass filtered mean velocities (Figs. S11C and S11D, bold lines) can also be used to characterize the movement of the specimen stage and adjust the time-series images to obtain drift-corrected time-series TEM images. The drift-corrected time-series TEM images (Fig. S11B) and the mean nanoparticle velocities calculated after the correction (Fig. S11E and S11F) show that the preferential nanoparticle movement in one direction caused by the specimen stage drift can be successfully corrected by using our method. When this procedure is applied to nanoparticles moving in liquid, the nanoparticle movements show no preferential direction (Fig. S12).

Calibration of nanoparticle trajectories utilizing the low-pass filtered mean velocity does not ensure that nanoparticle motion is free of bias. The effect of drift calibration on nanoparticle displacements can be monitored by calculating the mean nanoparticle displacement. It was found that the time-ensemble average, $\langle\overline{\Delta\mathbf{r}(t)}\rangle$, of drift-corrected nanoparticle displacements is close to zero compared to the result before calibration but still has finite values at long times (Fig. S13). Because of the nonvanishing mean displacement at long times, the mean square displacement, $\langle\overline{\Delta\mathbf{r}(t)^2}\rangle$, has slightly larger values than the variance, $\langle\overline{\delta\Delta\mathbf{r}(t)^2}\rangle\left[=\langle\overline{\Delta\mathbf{r}(t)^2}\rangle-\langle\overline{\Delta\mathbf{r}(t)}\rangle^2\right]$, of the nanoparticle displacement at long times (Fig. S14A). In fact, the difference between them is the same as the square of the mean nanoparticle displacement (Fig. S14B), indicating that the deviation of the mean square displacement from the variance originates from the nonzero mean displacement. In order to account for the fluctuation in nanoparticle displacements free of bias from the finite mean displacement, we considered the difference, $\delta\Delta\mathbf{r}_i(t)$, between nanoparticle displacement and mean nanoparticle displacement in the calculations of the variance of nanoparticle displacement and the non-Gaussian parameter. The number of nanoparticle

trajectories used for the calculation of the variance of nanoparticle displacement and the non-Gaussian parameter is sufficient to achieve statistically reliable results (Fig. S15).

S3. Off-lattice random walk model in dynamically heterogeneous environment

A. Generalized transport equation

In this subsection, we provide the derivation of the time-evolution equation of $p(\mathbf{r},\mathbf{\Gamma},t)$, which denotes the joint probability density that a random walker is located at position **r** and the environmental state is at $\mathbf{\Gamma}$ at time *t*. $p(\mathbf{r},\mathbf{\Gamma},t)$ can then be written as (*38*, *42*)

$$p(\mathbf{r},\mathbf{\Gamma},t)=\sum_{N=0}^{\infty}p_N(\mathbf{r})P_N(\mathbf{\Gamma},t) \tag{S3-1}$$

where $p_N(\mathbf{r})$ is the probability density that a random walker is placed at the position **r** after *N* jumps. In a spatially homogeneous environment, $p_N(\mathbf{r})$ can be expressed as the (*N*–1)-time spatial convolution of $p_{N=1}(\mathbf{r})\,[\equiv f(\mathbf{r})]$, i.e., $p_N(\mathbf{r})=\left[\prod_{i=2}^{N}\int d\mathbf{r}_{i-1}f(\mathbf{r}_i-\mathbf{r}_{i-1})\right]f(\mathbf{r}_1)$ with $\mathbf{r}_N$ being equivalent to **r**, the Fourier transform of which is given by $\tilde{p}_N(\mathbf{k})=\tilde{f}(\mathbf{k})^N$. Here, the Fourier transform, $\tilde{f}(\mathbf{k})$, of $f(\mathbf{r})$ is defined by $\tilde{f}(\mathbf{k})=\int d\mathbf{r}e^{i\mathbf{k}\cdot\mathbf{r}}f(\mathbf{r})$. In addition, on the right-hand side of Eq. (S3-1), $P_N(\mathbf{\Gamma},t)$ denotes the joint probability that the total number of jumps made by a random walker is *N* and the environmental state is at $\mathbf{\Gamma}$ at time *t*. $P_N(\mathbf{\Gamma},t)$ satisfies Sung and Silbey's generalized master equation (*43*):

$$\hat{\dot{P}}_N(\mathbf{\Gamma},s)=\hat{\kappa}_{\mathbf{\Gamma}}(s)\left[\hat{P}_{N-1}(\mathbf{\Gamma},s)-\hat{P}_N(\mathbf{\Gamma},s)\right]+L(\mathbf{\Gamma})\hat{P}_N(\mathbf{\Gamma},s) \tag{S3-2}$$

On the left-hand side of Eq. (S3-2), $\hat{\dot{P}}_N(\mathbf{\Gamma},s)$ designates the Laplace transform of $\dot{P}_N(\mathbf{\Gamma},t)[\equiv\partial_t P_N(\mathbf{\Gamma},t)]$ over *t*, where the Laplace transform, $\hat{h}(s)$, of a function, $h(t)$, is defined by $\hat{h}(s)=\int_0^\infty dte^{-st}h(t)$. On the right-hand side, the rate kernel, $\hat{\kappa}_{\mathbf{\Gamma}}(s)$, is related to the environment-coupled sojourn time distribution, $\psi_{\mathbf{\Gamma}}(t)$, as $\hat{\kappa}_{\mathbf{\Gamma}}(s)=s\hat{\psi}_{\mathbf{\Gamma}}(s)/[1-\hat{\psi}_{\mathbf{\Gamma}}(s)]$ in the Laplace domain

(*38*). $L(\mathbf{\Gamma})$ is the time evolution operator describing the dynamics of hidden environmental variables, $\mathbf{\Gamma}$, coupled to the random walker's motion.

In order to derive the time-evolution equation of $p(\mathbf{r},\mathbf{\Gamma},t)$, we take the first-order time derivative of Eq. (S3-1). The Fourier-Laplace transform of the resulting equation is given by

$$\hat{\tilde{p}}(\mathbf{k},\mathbf{\Gamma},s)=\sum_{N=0}^{\infty}\tilde{p}_N(\mathbf{k})\hat{P}_N(\mathbf{\Gamma},s) \tag{S3-3}$$

Substituting Eq. (S3-2) into Eq. (S3-3) and using the fact that $\hat{\tilde{p}}(\mathbf{k},\mathbf{\Gamma},s)=\sum_{N=0}^{\infty}\tilde{p}_N(\mathbf{k})\hat{P}_N(\mathbf{\Gamma},s)$ $=\sum_{N=0}^{\infty}\tilde{f}(\mathbf{k})^N\hat{P}_N(\mathbf{\Gamma},s)$ from Eq. (S3-1), we have

$$\hat{\tilde{p}}(\mathbf{k},\mathbf{\Gamma},s)=-\hat{\kappa}_{\mathbf{\Gamma}}(s)[1-\tilde{f}(\mathbf{k})]\hat{\tilde{p}}(\mathbf{k},\mathbf{\Gamma},s)+L(\mathbf{\Gamma})\hat{\tilde{p}}(\mathbf{k},\mathbf{\Gamma},s) \tag{S3-4}$$

In such an isotropic environment that $f(\mathbf{r})$ is a function only of $r(=|\mathbf{r}|)$, where r indicates the length of a single jump made by a random walker, $\tilde{f}(\mathbf{k})$ can be rewritten as

$$\begin{aligned}\tilde{f}(\mathbf{k}) &= \int d\mathbf{r}e^{i\mathbf{k}\cdot\mathbf{r}}f(\mathbf{r}) \\ &= \int_0^{\infty}drr^{d-1}\left[\gamma_{d-1}\int_0^{\pi}d\theta\sin^{d-2}\theta e^{ikr\cos\theta}\right]f(r) \\ &= (2\pi)^{d/2}k^{1-d/2}\int_0^{\infty}drr^{d/2}J_{d/2-1}(kr)f(r)\end{aligned} \tag{S3-5}$$

which is also a function only of the magnitude, k, of the wave vector, $\mathbf{k}$. In Eq. (S3-5), the second equality holds for the d-dimensional spherical coordinate system, where γ_d and θ respectively denote the dimension-dependent factor, $\gamma_d=2\pi^{d/2}/\Gamma(d/2)\left(=\gamma_{d-1}\int_0^{\pi}d\theta\sin^{d-2}\theta\right)$, with $\Gamma(z)$ being the gamma function defined by $\Gamma(z)=\int_0^{\infty}dx\,x^{z-1}e^{-x}$ and the angle between the two vectors, $\mathbf{k}$ and $\mathbf{r}$. $\gamma_d r^{d-1}dr$ indicates the volume of the shell enclosed by d-dimensional concentric spheres with radii r and $r+dr$. To obtain the final equation in Eq. (S3-5), we have used the following

relation: $\gamma_{d-1}\int_0^\pi d\theta \sin^{d-2}\theta e^{ikr\cos\theta} = (2\pi)^{d/2}(kr)^{1-d/2}J_{d/2-1}(kr)$, where $J_\nu(z)$ denotes the νth-order Bessel function of the first kind. Substituting the infinite series expression of $J_\nu(z)$ into Eq. (S3-5), the Maclaurin series of $\tilde{f}(\mathbf{k})$ can be easily obtained as

$$\tilde{f}(\mathbf{k}) = \sum_{n=0}^{\infty}\frac{k^n}{n!}\partial_k^n\tilde{f}(\mathbf{k})\Big|_{k=0} = \sum_{m=0}^{\infty}\frac{k^{2m}}{(2m)!}\left[(-1)^m\frac{(1/2)^{(m)}}{(d/2)^{(m)}}\langle r^{2m}\rangle\right] \tag{S3-6}$$

where $z^{(m)}$ denotes the rising factorial defined by $z^{(m)} = \Gamma(z+m)/\Gamma(z)$ and $\langle\mathbf{r}^q\rangle$ is the qth-order moment of $f(\mathbf{r})$, i.e., $\langle\mathbf{r}^q\rangle = \int d\mathbf{r}\mathbf{r}^q f(\mathbf{r})$. In Eq. (S3-6), only even q contributes to $\tilde{f}(\mathbf{k})$ because the odd-order moment of an unbiased symmetric distribution vanishes, explicitly, $\langle\mathbf{r}^{2m+1}\rangle = \int d\mathbf{r}r^{2m}f(r)\mathbf{r} = \mathbf{0}$. For even q (=2m), $\langle\mathbf{r}^q\rangle$ can be expressed as $\langle\mathbf{r}^q\rangle = \langle r^{2m}\rangle$ $= \int_0^\infty dr\gamma_d r^{d-1}r^{2m}f(r)$. From now on, we will use a new notation, $\langle l^{2m}\rangle$, in replacement of $\langle r^{2m}\rangle$ to avoid confusion with the displacement moment discussed in subsection B.

In the continuous, or small-k limit where only the first two terms on the right-hand side of the second equality in Eq. (S3-6) are kept, i.e., $\tilde{f}(\mathbf{k}) \cong 1 - k^2\langle l^2\rangle/2d$, Eq. (S3-4) reduces to the generalized diffusive transport equation (*38*):

$$\tilde{\hat{p}}(\mathbf{k},\mathbf{\Gamma},s) = -k^2\hat{\mathrm{D}}_{\mathbf{\Gamma}}(s)\hat{\tilde{p}}(\mathbf{k},\mathbf{\Gamma},s) + L(\mathbf{\Gamma})\hat{\tilde{p}}(\mathbf{k},\mathbf{\Gamma},s) \tag{S3-7}$$

where $\hat{\mathrm{D}}_{\mathbf{\Gamma}}(s)$ denotes the environment-dependent diffusion kernel defined by $\hat{\mathrm{D}}_{\mathbf{\Gamma}}(s) = \langle l^2\rangle\hat{\kappa}_{\mathbf{\Gamma}}(s)/2d$.

The formal solution of $\hat{\tilde{p}}(\mathbf{k},\mathbf{\Gamma},s)$ can be found from Eq. (S3-4). In Eq. (S3-4), $\tilde{\hat{p}}(\mathbf{k},\mathbf{\Gamma},s)$ can be written as $\tilde{\hat{p}}(\mathbf{k},\mathbf{\Gamma},s) = s\hat{p}(\mathbf{k},\mathbf{\Gamma},s) - p(\mathbf{k},\mathbf{\Gamma},0)$, where $p(\mathbf{k},\mathbf{\Gamma},0)$ is the Fourier transform of $p(\mathbf{r},\mathbf{\Gamma},0)$. Here, $p(\mathbf{r},\mathbf{\Gamma},0)$ is given by $p(\mathbf{r},\mathbf{\Gamma},0) = \delta(\mathbf{r}-\mathbf{r}_0)p_{st}(\mathbf{\Gamma})$ with $p_{st}(\mathbf{\Gamma})$ denoting the

stationary distribution of the environmental state, $\mathbf{\Gamma}$, defined by $L(\mathbf{\Gamma})p_{st}(\mathbf{\Gamma})=0$. With this initial condition at hand, the expression of $p(\mathbf{k},\mathbf{\Gamma},0)$ is then given by $p(\mathbf{k},\mathbf{\Gamma},0)=e^{i\mathbf{k}\cdot\mathbf{r}_0}p_{st}(\mathbf{\Gamma})$, which further reduces to $p(\mathbf{k},\mathbf{\Gamma},0)=p_{st}(\mathbf{\Gamma})$ by setting the initial position, $\mathbf{r}_0$, of a random walker to be the origin of the coordinate system, i.e., $\mathbf{r}_0=\mathbf{0}$. Finally, the formal solution of $\hat{\tilde{p}}(\mathbf{k},\mathbf{\Gamma},s)$ can be obtained as

$$\hat{\tilde{p}}(\mathbf{k},\mathbf{\Gamma},s)=\left[s-L(\mathbf{\Gamma})+\hat{\kappa}_{\mathbf{\Gamma}}(s)[1-\tilde{f}(\mathbf{k})]\right]^{-1}p_{st}(\mathbf{\Gamma}) \tag{S3-8}$$

When the dynamics of the environmental state, $\mathbf{\Gamma}$, and the $\mathbf{\Gamma}$-dependence of the rate kernel are modelled at an appropriate level, the analytical expression of Eq. (S3-8) can be found, which will be taken into account in subsection C.

In the fast environmental fluctuation limit, Eq. (S3-7) reduces to the $\mathbf{\Gamma}$-independent transport equation, $\dot{\hat{\tilde{p}}}(\mathbf{k},s)=-k^2\hat{\mathrm{D}}(s)\hat{\tilde{p}}(\mathbf{k},s)$, which corresponds to the generalized Fokker-Planck equation (GFPE) mentioned in ref. (*46*). In the case of the Fickian diffusion, the $\mathbf{\Gamma}$-independent diffusion kernel, $\hat{\mathrm{D}}(s)$, must read as the s-independent diffusion constant, which means that the GFPE becomes the simple diffusion equation describing only the Fickian and Gaussian diffusion, not applicable to the Fickian yet non-Gaussian diffusion, as discussed in ref. (*46*). Note here that the main transport equation presented in ref. (*38*) is not the GFPE but Eq. (S3-7) enabling a quantitative explanation of the non-Fickian and non-Gaussian transport dynamics as well as the Fikcian yet non-Gaussian transport dynamics. In ref. (*38*), it is never stated that the GFPE can be used to explain the Fickian yet non-Gaussian diffusion, which is misclaimed in ref. (*46*).

B. The first two moments of displacement

In this subsection, we calculate the first two nonvanishing moments, $\langle \mathbf{r}(t)^2 \rangle \left(= \langle r^2(t) \rangle \equiv \Delta_2(t) \right)$ and $\langle \mathbf{r}(t)^4 \rangle \left(= \langle r^4(t) \rangle \equiv \Delta_4(t) \right)$ of the displacement vector, $\mathbf{r}$, which are related to the $\mathbf{\Gamma}$-dependent displacement distribution, $p(\mathbf{r}, \mathbf{\Gamma}, t)$, as

$$\Delta_{q=2,4}(t) = \int d\mathbf{\Gamma} \Delta_{q=2,4}(\mathbf{\Gamma}, t) \tag{S3-9}$$

where $\Delta_q(\mathbf{\Gamma}, t)$ is defined by $\Delta_q(\mathbf{\Gamma}, t) = \int_0^\infty dr \gamma_d r^{d-1} r^q p(\mathbf{r}, \mathbf{\Gamma}, t)$. Taking the second and fourth derivatives of $\tilde{p}(\mathbf{k}, \mathbf{\Gamma}, t)$ with respect to k and setting $k = 0$ in the resulting equations, we have

$$\begin{aligned} \partial_k^q \tilde{p}(\mathbf{k}, \mathbf{\Gamma}, t)\big|_{k=0} &= \partial_k^q \int d\mathbf{r} e^{ikr\cos\theta} p(\mathbf{r}, \mathbf{\Gamma}, t)\big|_{k=0} \\ &= \int d\mathbf{r} \left(ir\cos\theta \right)^q p(\mathbf{r}, \mathbf{\Gamma}, t) \\ &= i^q \int_0^\infty dr r^{d-1} r^q \left[\gamma_{d-1} \int_0^\pi d\theta \sin^{d-2}\theta \cos^q\theta \right] p(\mathbf{r}, \mathbf{\Gamma}, t) \\ &= \begin{cases} -\Delta_2(\mathbf{\Gamma}, t)/d, & \text{for } q = 2 \\ 3\Delta_4(\mathbf{\Gamma}, t)/d(2+d), & \text{for } q = 4 \end{cases} \end{aligned} \tag{S3-10}$$

where θ is the angle between the two vectors, $\mathbf{k}$ and $\mathbf{r}$, defined by $\cos\theta = \mathbf{k} \cdot \mathbf{r}/kr$. In Eq. (S3-10), the third equality holds for the d-dimensional spherical coordinate system. To obtain the final equation in Eq. (S3-10), we have used the following relation: $\gamma_{d-1} \int_0^\pi d\theta \sin^{d-2}\theta \cos^q\theta = 2\pi^{\frac{d-1}{2}} \Gamma(\frac{1+q}{2}) / \Gamma(\frac{d+q}{2})$ for even q.

Applying the operation, $-d\partial_k^2(\cdots)\big|_{k=0}$, to both sides of Eq. (S3-4) and using Eqs. (S3-6) and (S3-10), we obtain

$$s\hat{\Delta}_2(\mathbf{\Gamma}, s) = 2d\hat{\mathrm{D}}_{\mathbf{\Gamma}}(s)\hat{\tilde{p}}(0, \mathbf{\Gamma}, s) + L(\mathbf{\Gamma})\hat{\Delta}_2(\mathbf{\Gamma}, s) \tag{S3-11}$$

with $\hat{\mathrm{D}}_{\mathbf{\Gamma}}(s)$ denoting the $\mathbf{\Gamma}$-dependent diffusion kernel defined by $\hat{\mathrm{D}}_{\mathbf{\Gamma}}(s) = \langle l^2 \rangle \hat{\kappa}_{\mathbf{\Gamma}}(s)/2d$. Using the fact that $\hat{\tilde{p}}(0,\mathbf{\Gamma},s) = \int d\mathbf{r}\hat{p}(\mathbf{r},\mathbf{\Gamma},s) = p_{st}(\mathbf{\Gamma})/s$, we can obtain the expression of $\hat{\Delta}_2(\mathbf{\Gamma},s)$ from Eq. (S3-11), which is given by

$$\hat{\Delta}_2(\mathbf{\Gamma},s) = 2d[s - L(\mathbf{\Gamma})]^{-1} \frac{\hat{\mathrm{D}}_{\mathbf{\Gamma}}(s) p_{st}(\mathbf{\Gamma})}{s} \tag{S3-12}$$

Using the property of the Dirac delta function and $\hat{G}(\mathbf{\Gamma},s \mid \mathbf{\Gamma}_0) = [s - L(\mathbf{\Gamma})]^{-1}\delta(\mathbf{\Gamma} - \mathbf{\Gamma}_0)$, where $\hat{G}(\mathbf{\Gamma},s \mid \mathbf{\Gamma}_0)$ denotes the Laplace transform of the propagator, $G(\mathbf{\Gamma},t \mid \mathbf{\Gamma}_0)$, or the conditional probability density that the environment is at state $\mathbf{\Gamma}$ at time *t*, given that the environment was at state $\mathbf{\Gamma}_0$ at time 0, Eq. (S3-12) can be rewritten as

$$\begin{aligned} \hat{\Delta}_2(\mathbf{\Gamma},s) &= 2d \int d\mathbf{\Gamma}_0 [s - L(\mathbf{\Gamma})]^{-1} \delta(\mathbf{\Gamma} - \mathbf{\Gamma}_0) \frac{\hat{\mathrm{D}}_{\mathbf{\Gamma}_0}(s) p_{st}(\mathbf{\Gamma}_0)}{s} \\ &= 2d \int d\mathbf{\Gamma}_0 \hat{G}(\mathbf{\Gamma},s \mid \mathbf{\Gamma}_0) \frac{\hat{\mathrm{D}}_{\mathbf{\Gamma}_0}(s) p_{st}(\mathbf{\Gamma}_0)}{s}. \end{aligned} \tag{S3-13}$$

Integrating both sides of Eq. (S3-13) over $\mathbf{\Gamma}$ and using the normalization condition, $\int d\mathbf{\Gamma}\hat{G}(\mathbf{\Gamma},s \mid \mathbf{\Gamma}_0) = 1/s$, we finally obtain the expression of the mean square displacement, $\hat{\Delta}_2(s)\left[= \int d\mathbf{\Gamma}\hat{\Delta}_2(\mathbf{\Gamma},s)\right]$, in the Laplace domain:

$$\hat{\Delta}_2(s) = \frac{2d}{s^2} \langle \hat{\mathrm{D}}_{\mathbf{\Gamma}}(s) \rangle, \tag{S3-14}$$

where $\langle \hat{\mathrm{D}}_{\mathbf{\Gamma}}(s) \rangle$ denotes the mean diffusion kernel defined by $\langle \hat{\mathrm{D}}_{\mathbf{\Gamma}}(s) \rangle = \int d\mathbf{\Gamma} \hat{\mathrm{D}}_{\mathbf{\Gamma}}(s) p_{st}(\mathbf{\Gamma})$. Equation (S3-14) is equivalent to the expression of $\hat{\Delta}_2(s)$ given in ref. (*38*).

Applying the operation, $d(2+d)\partial_k^4(\cdots)\big|_{k=0}/3$, to both sides of Eq. (S3-4) and using Eqs. (S3-6) and (S3-10), we obtain

$$s\hat{\Delta}_4(\mathbf{\Gamma},s)=\frac{8d(d+2)}{s}\hat{\mathrm{D}}_{\mathbf{\Gamma}}(s)[s-L(\mathbf{\Gamma})]^{-1}\hat{\mathrm{D}}_{\mathbf{\Gamma}}(s)p_{st}(\mathbf{\Gamma})$$
$$+\frac{(4+d)(24-12d+2d^2+d^3)}{96}\frac{\langle l^4\rangle}{\langle l^2\rangle}2d\hat{\mathrm{D}}_{\mathbf{\Gamma}}(s)\,p_{st}(\mathbf{\Gamma})/s+L(\mathbf{\Gamma})\hat{\Delta}_4(\mathbf{\Gamma},s) \quad \text{(S3-15)}$$

Solving Eq. (S3-15) with respect to $\hat{\Delta}_4(\mathbf{\Gamma},s)$, we have

$$\hat{\Delta}_4(\mathbf{\Gamma},s)=\frac{8d(d+2)}{s}[s-L(\mathbf{\Gamma})]^{-1}\hat{\mathrm{D}}_{\mathbf{\Gamma}}(s)[s-L(\mathbf{\Gamma})]^{-1}\hat{\mathrm{D}}_{\mathbf{\Gamma}}(s)p_{st}(\mathbf{\Gamma})$$
$$+\frac{(4+d)(24-12d+2d^2+d^3)}{96}\frac{\langle l^4\rangle}{\langle l^2\rangle}2d[s-L(\mathbf{\Gamma})]^{-1}\hat{\mathrm{D}}_{\mathbf{\Gamma}}(s)\,p_{st}(\mathbf{\Gamma})/s \quad \text{(S3-16)}$$

Using the fact that $\hat{G}(\mathbf{\Gamma},s\,|\,\mathbf{\Gamma}_0)=[s-L(\mathbf{\Gamma})]^{-1}\delta(\mathbf{\Gamma}-\mathbf{\Gamma}_0)$, Eq. (S3-16) can be rewritten as

$$\hat{\Delta}_4(\mathbf{\Gamma},s)=\frac{8d(d+2)}{s}\int d\mathbf{\Gamma}_1\int d\mathbf{\Gamma}_0\hat{G}(\mathbf{\Gamma},s\,|\,\mathbf{\Gamma}_1)\hat{\mathrm{D}}_{\mathbf{\Gamma}_1}(s)\hat{G}(\mathbf{\Gamma}_1,s\,|\,\mathbf{\Gamma}_0)\hat{\mathrm{D}}_{\mathbf{\Gamma}_0}(s)p_{st}(\mathbf{\Gamma}_0)$$
$$+\frac{(4+d)(24-12d+2d^2+d^3)}{96}\frac{\langle l^4\rangle}{\langle l^2\rangle}2d\int d\mathbf{\Gamma}_0\hat{G}(\mathbf{\Gamma},s\,|\,\mathbf{\Gamma}_0)\frac{\hat{\mathrm{D}}_{\mathbf{\Gamma}_0}(s)p_{st}(\mathbf{\Gamma}_0)}{s} \quad \text{(S3-17)}$$

The integration of Eq. (S3-17) over $\mathbf{\Gamma}$ yields the expression of $\hat{\Delta}_4(s)\left[=\int d\mathbf{\Gamma}\hat{\Delta}_4(\mathbf{\Gamma},s)\right]$:

$$\hat{\Delta}_4(s)=\frac{8d(d+2)}{s^2}\int d\mathbf{\Gamma}\int d\mathbf{\Gamma}_0\hat{\mathrm{D}}_{\mathbf{\Gamma}}(s)\hat{G}(\mathbf{\Gamma},s\,|\,\mathbf{\Gamma}_0)\hat{\mathrm{D}}_{\mathbf{\Gamma}_0}(s)p_{st}(\mathbf{\Gamma}_0)$$
$$+\frac{(4+d)(24-12d+2d^2+d^3)}{96}\frac{\langle l^4\rangle}{\langle l^2\rangle}\hat{\Delta}_2(s) \quad \text{(S3-18)}$$

where Eqs. (S3-13) and (S3-14) have been used. Equation (S3-18) can be rearranged to

$$\hat{\Delta}_4(s)=\frac{8d(d+2)}{s^3}\langle\hat{\mathrm{D}}_{\mathbf{\Gamma}}(s)\rangle^2\left[1+s\hat{C}_{\mathrm{D}}(s)\right]+\frac{(4+d)(24-12d+2d^2+d^3)}{96}\frac{\langle l^4\rangle}{\langle l^2\rangle}\hat{\Delta}_2(s) \quad \text{(S3-19)}$$

where $\hat{C}_{\mathrm{D}}(s)$ denotes the Laplace transform of the generalized time correlation function defined by

$$\hat{C}_{\mathrm{D}}(s)=\int d\mathbf{\Gamma}\int d\mathbf{\Gamma}_0\frac{\delta\hat{\mathrm{D}}_{\mathbf{\Gamma}}(s)}{\langle\hat{\mathrm{D}}_{\mathbf{\Gamma}}(s)\rangle}\hat{G}(\mathbf{\Gamma},s\,|\,\mathbf{\Gamma}_0)\frac{\delta\hat{\mathrm{D}}_{\mathbf{\Gamma}_0}(s)}{\langle\hat{\mathrm{D}}_{\mathbf{\Gamma}_0}(s)\rangle}p_{st}(\mathbf{\Gamma}_0) \quad \text{(S3-20)}$$

In Eq. (S3-20), $\delta\hat{D}_{\Gamma}(s)$ denotes the deviation, $\delta\hat{\mathrm{D}}_{\boldsymbol{\Gamma}}(s)=\hat{\mathrm{D}}_{\boldsymbol{\Gamma}}(s)-\langle\hat{\mathrm{D}}_{\boldsymbol{\Gamma}}(s)\rangle$, of the diffusion kernel from its average. Substituting $\langle\hat{\mathrm{D}}_{\boldsymbol{\Gamma}}(s)\rangle=s^2\hat{\Delta}_2(s)/2d$, or Eq. (S3-14), into Eq. (S3-19), we finally obtain

$$\hat{\Delta}_4(s)=\left(1+\frac{2}{d}\right)2s\hat{\Delta}_2(s)^2\left[1+s\hat{C}_{\mathrm{D}}(s)\right]+\frac{(4+d)(24-12d+2d^2+d^3)}{96}\frac{\langle l^4\rangle}{\langle l^2\rangle}\hat{\Delta}_2(s) \quad \text{(S3-21)}$$

In the small-jump length (l) limit, the second term on the right-hand side of Eq. (S3-21) vanishes, resulting in the same expression for $\hat{\Delta}_4(s)$ as in ref. (*38*). Before ending this section, it should be noted that the observed nanoparticle motion in the GLC shows ergodic behavior; both mean square displacements calculated in the two different ways, the ensemble average and the time-ensemble average, linearly increase with time and are the same as each other (Fig. S19). The theoretical results based on the ensemble average can thus be compared with the experimental results based on the time-ensemble average.

C. Explicit model of diffusion kernel and environmental dynamics

In this subsection, we provide an explicit model of the environmental state ($\boldsymbol{\Gamma}$)-dependence of the diffusion kernel and the dynamics of $\boldsymbol{\Gamma}$ in accordance with the experimental data presented in Fig. 2 of the main text. As shown in Fig. 2A, the variance of nanoparticle displacements linearly increases with time. In our theory considering a random walker's motion without any bias in a specific direction, the mean square displacement consistent with the experimental result is given by $\Delta_2(t)=2d\langle D\rangle t$ with $\langle D\rangle$ denoting the mean diffusion coefficient, or $\hat{\Delta}_2(s)=2d\langle D\rangle/s^2$ in the Laplace domain. From comparison with Eq. (S3-14), it is found that the ($\boldsymbol{\Gamma}$, s)-dependent diffusion kernel, $\hat{\mathrm{D}}_{\boldsymbol{\Gamma}}(s)$, must be independent of s in our case, which can be achieved when $\psi_{\boldsymbol{\Gamma}}(t)$ is given by an exponential distribution with the $\boldsymbol{\Gamma}$-dependent jump rate, $\kappa_{\boldsymbol{\Gamma}}$, i.e., $\psi_{\boldsymbol{\Gamma}}(t)=\kappa_{\boldsymbol{\Gamma}}e^{-t\kappa_{\boldsymbol{\Gamma}}}$,

or $\hat{\psi}_{\mathbf{\Gamma}}(s) = (1 + s/\kappa_{\mathbf{\Gamma}})^{-1}$ in the Laplace domain, resulting in $\hat{\kappa}_{\mathbf{\Gamma}}(s) = s\hat{\psi}_{\mathbf{\Gamma}}(s)/[1 - \hat{\psi}_{\mathbf{\Gamma}}(s)] = \kappa_{\mathbf{\Gamma}}$. Subsequently, $\hat{\mathrm{D}}_{\mathbf{\Gamma}}(s)$ becomes the $\mathbf{\Gamma}$-dependent diffusion coefficient, explicitly, $\hat{\mathrm{D}}_{\mathbf{\Gamma}}(s)$ $= \langle l^2 \rangle \hat{\kappa}_{\mathbf{\Gamma}}(s)/2d = \langle l^2 \rangle \kappa_{\mathbf{\Gamma}}/2d = D_{\mathbf{\Gamma}}$. $D_{\mathbf{\Gamma}}$, or D undergoes a time-dependent fluctuation, depending on the dynamics of $\mathbf{\Gamma}$.

How diffusion coefficients are distributed is one of important inputs required to model the dynamics of the environmental state. As shown in Fig. 2C, the nanoparticle diffusion coefficient follows a gamma distribution, $P_D(D) = D^{a-1}e^{-D/b}/b^a\Gamma(a)$ with ab and ab^2 being the mean, $\langle D \rangle$, and variance, $\langle \delta D^2 \rangle$, respectively. A use of lognormal distribution can also be considered, but the gamma distribution model makes it possible to obtain the analytical expression of the displacement distribution as will be shown below. With $\langle D \rangle = ab$ at hand, $P_D(D)$ can be rewritten as

$$P_D(D) = \frac{1}{(\langle D \rangle/a)^a \Gamma(a)} D^{a-1} e^{-aD/\langle D \rangle} \tag{S3-22}$$

In order to model the fluctuation of the diffusion coefficient, one can make use of the fact that the sum, $\sum_{i=1}^{n} \Gamma_i^2 (\equiv Y)$, of n squared Gaussian random variables, $\{\Gamma^2_{1 \le i \le n}\}$, follows a chi-squared distribution:

$$P_Y(Y) = \frac{1}{2^{n/2}\Gamma(n/2)} Y^{n/2-1} e^{-\frac{1}{2}Y} \tag{S3-23}$$

where each Gaussian random variable contributing to Y has zero mean and unit variance, and they are mutually independent of each other, in short, $\langle \Gamma_i \Gamma_j \rangle = \delta_{ij}$. Equating Eq. (S3-23) with Eq. (S3-22) with their own differentials, i.e., $P_D(D)dD = P_Y(Y)dY$, it is found that the shape parameter, a, of the gamma distribution [Eq. (S3-22)] and the diffusion coefficient, D, are respectively given by

$$a = n/2 \tag{S3-24A}$$

$$D = \frac{\langle D \rangle}{n} Y = \frac{\langle D \rangle}{n} \sum_{i=1}^{n} \Gamma_i^2 \tag{S3-24B}$$

Assuming that $\{\Gamma_i\}(=\boldsymbol{\Gamma})$ are stationary Markovian processes, also known as Ornstein-Uhlenbeck processes, the time-evolution operator, $L(\boldsymbol{\Gamma})$, of the environmental variables, $\boldsymbol{\Gamma}$, can be explicitly written as

$$L(\boldsymbol{\Gamma}) = \sum_{i=1}^{n} L_i(\Gamma_i);\ L_i(\Gamma_i) = \lambda_i \frac{\partial}{\partial \Gamma_i} \left(\frac{\partial}{\partial \Gamma_i} + \Gamma_i \right) \tag{S3-25}$$

where $L_i(\Gamma_i)$ denotes the time-evolution operator of the *i*th Ornstein-Uhlenbeck mode, Γ_i. λ_i is the relaxation rate of the time correlation function for Γ_i, given by $\langle \Gamma_i(t)\Gamma_i(t') \rangle = e^{-\lambda_i |t-t'|}$. Substituting Eqs. (S3-24) and (S3-25) into Eq. (S3-8) with $\hat{\kappa}_{\boldsymbol{\Gamma}}(s) = 2d\hat{\mathrm{D}}_{\boldsymbol{\Gamma}}(s) \big/ \langle l^2 \rangle = 2dD \big/ \langle l^2 \rangle$, we have, in the time domain,

$$\tilde{p}(\mathbf{k}, \boldsymbol{\Gamma}, t) = e^{t \sum_{i=1}^{n} \left[L_i(\Gamma_i) - \kappa_c [1 - \tilde{f}(\mathbf{k})] \Gamma_i^2 \right]} p_{st}(\boldsymbol{\Gamma}) \tag{S3-26}$$

where κ_c is the constant defined by $\kappa_c = 2d\langle D \rangle \big/ n\langle l^2 \rangle$, which can be rewritten as $\kappa_c = db \big/ \langle l^2 \rangle$ using $\langle D \rangle = ab$ and Eq. (S3-24A). In Eq. (S3-26), the stationary distribution, $p_{st}(\boldsymbol{\Gamma})$, is given by the product of *n* individual Gaussian distributions, i.e., $p_{st}(\boldsymbol{\Gamma}) = \prod_{i=1}^{n} p_{st,i}(\Gamma_i)$ $= \prod_{i=1}^{n} \left[e^{-\Gamma_i^2/2} \big/ (2\pi)^{1/2} \right]$. The Fourier transform, $\tilde{p}(\mathbf{k}, t)$, of the normalized displacement distribution, $p(\mathbf{r}, t)$, is then obtained by integrating both sides of Eq. (S3-26) over $\boldsymbol{\Gamma}$:

$$\begin{aligned} \tilde{p}(\mathbf{k}, t) &= \int d\boldsymbol{\Gamma} \tilde{p}(\mathbf{k}, \boldsymbol{\Gamma}, t) = \int d\boldsymbol{\Gamma} e^{t \sum_{i=1}^{n} \left[L_i(\Gamma_i) - \kappa_c [1 - \tilde{f}(\mathbf{k})] \Gamma_i^2 \right]} p_{st}(\boldsymbol{\Gamma}) \\ &= \prod_{i=1}^{n} \int_{-\infty}^{\infty} d\Gamma_i e^{t \sum_{i=1}^{n} \left[L_i(\Gamma_i) - \kappa_c [1 - \tilde{f}(\mathbf{k})] \Gamma_i^2 \right]} p_{st,i}(\Gamma_i) \\ &= \prod_{i=1}^{n} \left[\frac{4\mu_{k,i} e^{-(\mu_{k,i} - 1)\lambda_i t}}{(\mu_{k,i} + 1)^2 - (\mu_{k,i} - 1)^2 e^{-2\mu_{k,i}\lambda_i t}} \right]^{1/2} \end{aligned} \tag{S3-27}$$

where $\mu_{k,i}$ is defined by $\mu_{k,i} = (1 + 4\kappa_c[1 - \tilde{f}(\mathbf{k})]/\lambda_i)^{1/2} = (1 + 4db[1 - \tilde{f}(\mathbf{k})]/\langle l^2 \rangle \lambda_i)^{1/2}$. In Eq. (S3-27), we have employed the result given in ref. (*44*). to obtain the final equation. For simplicity, the relaxation rates, λ_i's, are here assumed to be the same as each other, i.e., $\lambda_i = \lambda = \tau^{-1}$. From Eq. (S3-27), we finally obtain the following expression of $\tilde{p}(\mathbf{k},t)$:

$$\tilde{p}(\mathbf{k},t) = \left[\frac{4\mu_k e^{-(\mu_k - 1)t/\tau}}{(\mu_k + 1)^2 - (\mu_k - 1)^2 e^{-2\mu_k t/\tau}} \right]^{n/2} ; \ \mu_k = \left(1 + \frac{4db\tau}{\langle l^2 \rangle} [1 - \tilde{f}(\mathbf{k})] \right)^{1/2} \tag{S3-28}$$

When $d = 2$, Eq. (S3-28) with Eq. (S3-24A) is equivalent to Eq. (1B) presented in the main text.

As shown in Eq. (S3-28), the *k*-dependence of $\tilde{p}(\mathbf{k},t)$ is determined by $\tilde{f}(\mathbf{k})$ so that we need to explicitly model the distribution, $f(l)$, of the jump length, *l*. In Fig. S20, it is shown that the distribution of the jump length, or the distance a nanoparticle travels in the two-dimensional field of view during the experimental time resolution follows an exponential distribution, $f(l) = e^{-l/l_c}/2\pi l_c^2$ with l_c denoting the characteristic jump length. Using Eq. (S3-5) with $d = 2$, the Fourier transform, $\tilde{f}(\mathbf{k})$, of $f(l) = e^{-l/l_c}/2\pi l_c^2$ is calculated as

$$\tilde{f}(\mathbf{k}) = (1 + k^2 l_c^2)^{-3/2} \tag{S3-29}$$

The displacement distribution, $p(\mathbf{r},t)$, can be calculated by performing the inverse Fourier transform of Eq. (S3-28):

$$p(\mathbf{r},t) = \frac{r^{1-d/2}}{(2\pi)^{d/2}} \int_0^\infty dk k^{d/2} J_{d/2-1}(kr) \tilde{p}(\mathbf{k},t) \tag{S3-30}$$

which corresponds to the inversion of the radial Fourier transform defined with Eq. (S3-5). When $d = 2$, Eq. (S3-30) reads as

$$p(\mathbf{r},t) = \frac{1}{2\pi} \int_0^\infty dk k J_0(kr) \tilde{p}(\mathbf{k},t) \tag{S3-31}$$

the short-time limiting expression of which is given by $p(\mathbf{r},0) = (2\pi)^{-1}\int_0^\infty dkkJ_0(kr)\tilde{p}(\mathbf{k},0)$ $= (2\pi)^{-1}\int_0^\infty dkkJ_0(kr) = (2\pi r)^{-1}\delta(r)$. Although $\int_0^\infty dkkJ_0(kr)$ is equal to zero for nonzero *r*, the numerical estimation of $\int_0^\infty dkkJ_0(kr)$ is not well-defined because $kJ_0(kr)$ oscillates over *k* in such a divergent manner that its amplitude keeps increasing with *k*. In the large-*k* limit where $\tilde{f}(\mathbf{k})$ given by Eq. (S3-29) vanishes, Eq. (S3-28) becomes independent of *k* so that the integrand in Eq. (S3-31) follows a divergent oscillatory tail, $kJ_0(kr)$, resulting in the failure of the numerical estimation of Eq. (S3-31). To overcome this numerical problem in the calculation of Eq. (S3-31), we employ the $[M+4/M]$-Padé approximant to $1-\tilde{f}(\mathbf{k})$ with Eq. (S3-29) (*45*), which diverges as $1-\tilde{f}(\mathbf{k}) \sim k^4$ at large *k*, making the *k*-integration in Eq. (S3-31) numerically convergent. The $[M+2/M]$-Padé approximant to $1-\tilde{f}(\mathbf{k})$ becomes negative at large *k*, which is unacceptable to $\tilde{p}(\mathbf{k},t)$. With the $[M+4/M]$-Padé approximant to $1-\tilde{f}(\mathbf{k})$, a use of larger *M* yields more exact estimation of $p(\mathbf{r},t)$ at small *r*. In Fig. 2E and 2F, we have used *M* = 100 to calculate Eq. (S3-31) with Eqs. (S3-28) and (S3-29). In Fig. 2F, the small pixel limit of the nanoparticle displacement distribution was obtained by calculating Eq. (S3-31) with Eqs. (S3-28) and (S3-29), and $1-\tilde{f}(\mathbf{k}) \cong k^2\langle l^2\rangle/2d = k^2\langle l^2\rangle/4$.

The non-Gaussian character of Eq. (S3-31) with Eqs. (S3-28) and (S3-29) can be captured by the non-Gaussian parameter (NGP), $\alpha_2(t)$, which is defined by $\alpha_2(t) = (1+\frac{2}{d})^{-1}\Delta_4(t)/\Delta_2(t)^2 - 1$ (*39*, *40*). For Gaussian displacement distributions, $\alpha_2(t)$ is identical to zero. Nonzero positive NGP reflects the heterogeneous transport dynamics of a tracer particle (*38*). To calculate the NGP, we need the explicit expression of $\Delta_2(t)$ and $\Delta_4(t)$. In the present model for the diffusion kernel

and the environmental dynamics, which is characterized by Eqs. (S3-24) and (S3-25), $\Delta_2(t)$ is simply given by $\Delta_2(t) = 2d\langle D\rangle t$. Substituting the Laplace transform, $\hat{\Delta}_2(s)$, of $\Delta_2(t)$, given by $\hat{\Delta}_2(s) = 2d\langle D\rangle / s^2$ into Eq. (S3-21) and performing the inverse Laplace transform of the resulting equation, we have

$$\begin{aligned}\Delta_4(t) = &\left(1+\frac{2}{d}\right)8d^2\langle D\rangle^2\left[\frac{1}{2}t^2 + \int_0^t dt'(t-t')C_{\mathrm{D}}(t')\right] \\ &+ \frac{(4+d)(24-12d+2d^2+d^3)}{96}\frac{\langle l^4\rangle}{\langle l^2\rangle}2d\langle D\rangle t\end{aligned} \tag{S3-32}$$

where the diffusion kernel correlation function, $C_{\mathrm{D}}(t)$, in the time domain can be explicitly calculated by using Eqs. (S3-24B) and (S3-25) in Eq. (S3-20). With Eq. (S3-24B) at hand, the time-domain expression of Eq. (S3-20) can be written as

$$\begin{aligned}C_{\mathrm{D}}(t) &= \frac{1}{n^2}\left[\sum_{i=1}^{n}\sum_{j=1}^{n}\int d\mathbf{\Gamma}\int d\mathbf{\Gamma}_0\Gamma_i^2 G(\mathbf{\Gamma},t\,|\,\mathbf{\Gamma}_0)\Gamma_j^2 p_{st}(\mathbf{\Gamma}_0)\right]-1 \\ &= \frac{1}{n^2}\sum_{i=1}^{n}\sum_{j=1}^{n}\left[\langle\Gamma_i^2(t)\Gamma_j^2(0)\rangle - 1\right]\end{aligned} \tag{S3-33}$$

In Eq. (S3-33), enjoying the fact that $\{\Gamma_i\}$ are mutually independent Gaussian random variables, the fourth-order correlation, $\langle\Gamma_i(t)\Gamma_i(t)\Gamma_j(0)\Gamma_j(0)\rangle$, can be easily calculated as

$$\begin{aligned}\langle\Gamma_i(t)\Gamma_i(t)\Gamma_j(0)\Gamma_j(0)\rangle &= \langle\Gamma_i(t)\Gamma_i(t)\rangle\langle\Gamma_j(0)\Gamma_j(0)\rangle + 2\langle\Gamma_i(t)\Gamma_j(0)\rangle\langle\Gamma_i(t)\Gamma_j(0)\rangle \\ &= 1 + 2\delta_{ij}e^{-2t/\tau}\end{aligned} \tag{S3-34}$$

With this result, Eq. (S3-33) further reduces to

$$C_{\mathrm{D}}(t) = \frac{2}{n}e^{-2t/\tau} = \eta_D^2 e^{-2t/\tau} \tag{S3-35}$$

with η_D^2 denoting the relative variance of D, i.e., $\eta_D^2 = \langle\delta D^2\rangle / \langle D\rangle^2$. Finally, we obtain the explicit expression of the NGP, which is given by

$$\alpha_2(t) = \frac{(4+d)(24-12d+2d^2+d^3)}{192(2+d)} \frac{\langle l^4 \rangle / \langle l^2 \rangle}{\langle D \rangle t} + \eta_D^2 \frac{2(t/\tau) - 1 + e^{-2t/\tau}}{2(t/\tau)^2} \quad \text{(S3-36)}$$

where the second- and fourth-order moments, $\langle l^2 \rangle$ and $\langle l^4 \rangle$, of the jump length distribution, $f(l)\left(= e^{-l/l_c} / 2\pi l_c^2\right)$, are respectively calculated as $\langle l^2 \rangle = 6l_c^2$ and $\langle l^4 \rangle = 120 l_c^4$. The two-dimensional version of Eq. (S3-36) is presented as Eq. (1A) in the main text.

Equation (S3-36) for the non-Gaussian parameter can be used to find the value of the time scale, τ, of the diffusion coefficient fluctuation. In Eq. (S3-36), values of $\langle D \rangle$ and η_D^2 are obtained from diffusion coefficients of individual nanoparticles estimated from the variance of the displacement at times shorter than one second (see Figs. 1D and 1F); $\langle D \rangle = 0.12$ nm^2/s and $\eta_D^2 =$ 0.26. The value of the characteristic jump length, l_c, is obtained as $l_c = 0.09$ nm from the best fit of $f(l)\left(= e^{-l/l_c} / 2\pi l_c^2\right)$ to the experimental data for the jump length distribution (see Fig. S20). The value of τ is obtained as $\tau = 3.58$ seconds from the best fit of Eq. (S3-36) to the experimental data for the NGP. In Eq. (S3-28), the number, *n*, of the Ornstein-Uhlenbeck modes is chosen to be eight, considering the relation between *n* and η_D^2 in the present model, given by $\eta_D^2 = 2/n$.

S4. Kinetics of two-step coalescence between ligand-passivated nanoparticles

A. Two-step coalescence model

In this subsection, we deal with how the survival probability, $S(t \mid r_0)$, that a pair of nanoparticles do not coalesce by time *t* are related to the distributions of the time elapsed at each step in the two-step coalescence model discussed in Fig. 5 of the main text. At first, let $\psi(t \mid r_0)$ denote the distribution of time taken for a pair of nanoparticles initially distant by r_0 to merge together. In addition, the distribution of time taken for a pair of nanoparticles initially distant by r_0 to form the complex at contact separation, σ, and the lifetime distribution of the encounter complex are respectively denoted by $\psi_1(t \mid r_0)$ and $\psi_2(t)$, as presented in the main text. $\psi(t \mid r_0)$ can then be expressed as the time convolution of $\psi_1(t \mid r_0)$ and $\psi_2(t)$:

$$\psi(t \mid r_0) = \int_0^t dt' \psi_2(t-t') \psi_1(t' \mid r_0) \tag{S4-1}$$

whose Laplace-domain expression is given by

$$\hat{\psi}(s \mid r_0) = \hat{\psi}_1(s \mid r_0) \hat{\psi}_2(s) \tag{S4-2}$$

Using the relation between $S(t \mid r_0)$ and $\psi(t \mid r_0)$, i.e., $S(t \mid r_0) = \int_t^\infty dt' \psi(t' \mid r_0)$ in the time domain, or $\hat{S}(s \mid r_0) = s^{-1}\left[1 - \hat{\psi}(s \mid r_0)\right]$ in the Laplace domain, $\hat{S}(s \mid r_0)$ can be written from Eq. (S4-2) as

$$\begin{aligned} \hat{S}(s \mid r_0) &= \frac{1 - \hat{\psi}_2(s) \hat{\psi}_1(s \mid r_0)}{s} \\ &= \hat{S}_2(s) + \hat{\psi}_2(s) \hat{S}_1(s \mid r_0) \end{aligned} \tag{S4-3}$$

where $\hat{S}_1(s \mid r_0)$ and $\hat{S}_2(s)$ respectively denote the Laplace-transformed survival probabilities related to $\hat{\psi}_1(s \mid r_0)$ and $\hat{\psi}_2(s)$ as $\hat{S}_1(s \mid r_0) = s^{-1}\left[1 - \hat{\psi}_1(s \mid r_0)\right]$ and $\hat{S}_2(s) = s^{-1}\left[1 - \hat{\psi}_2(s)\right]$ in the

same way as the relation between $\hat{S}(s \mid r_0)$ and $\hat{\psi}(s \mid r_0)$. The inverse Laplace transform of Eq. (S4-3) yields

$$S(t \mid r_0) = S_2(t) + \int_0^t dt' \psi_2(t-t') S_1(t' \mid r_0) \tag{S4-4}$$

When $\psi_2(t)$ is an exponential distribution givne by $\psi_2(t) = ke^{-tk}$, Eq. (S4-4) reads as

$$S(t \mid r_0) = e^{-kt} + k\int_0^t dt' e^{-k(t-t')} S_1(t' \mid r_0) \tag{S4-5}$$

In Eq. (S4-4) or (S4-5), the explicit expression of $S_1(t \mid r_0)$ hinges on the first encounter dynamics of coalescing nanoparticle pairs in the presence of fluctuating diffusivity, which will be treated in details in the next subsection.

B. Radially symmetric propagator and associated survival probability

On the basis of the transport model described in section S3, we derive the radially symmetric propagator, $p_1(r,t \mid r_0)$, which is the conditional probability density that a random walker is distant from the coordinate origin by *r* at time *t*, given that the initial distance of the random walker was r_0 at time 0. Here, $p_1(r,t \mid r_0)$ satisfies the absorbing boundary condition, $p_1(\sigma,t \mid r_0) = 0$, at contact separation, σ. The whole space integration of $p_1(r,t \mid r_0)$ is then nothing but $S_1(t \mid r_0)$:

$$S_1(t \mid r_0) = \int_\sigma^\infty dr \gamma_d r^{d-1} p_1(r,t \mid r_0) \tag{S4-6}$$

At first, let us consider the boundary-free propagator, $p(r,t \mid r_0)$ in the two-dimensional space. In Eq. (S3-31), $p(\mathbf{r},t)$ is the displacement distribution, where *r* is just the magnitude of the displacement vector. When the initial position, $\mathbf{r}_0$, of a random walker is separated from the coordinate origin, the magnitude of the displacement vector is given by $R = \sqrt{r^2 + r_0^2 - 2rr_0\cos\theta}$ with θ denoting the angle defined between two vectors, $\mathbf{r}$ and $\mathbf{r}_0$. In replacement of *r* with *R*, the

displacement distribution, $p(\mathbf{r},t)$, given in Eq. (S3-31) becomes the conditional probability density, $p(\mathbf{r},t\,|\,\mathbf{r}_0)$, which is given by

$$p(\mathbf{r},t\,|\,\mathbf{r}_0)=\frac{1}{2\pi}\int_0^\infty dkkJ_0(kR)\tilde{p}(\mathbf{k},t) \tag{S4-7}$$

The radially symmetric propagator, $p(r,t\,|\,r_0)$, is then obtained by averaging Eq. (S4-7) over θ as

$$\begin{aligned} p(r,t\,|\,r_0)&=\frac{1}{2\pi}\int_0^{2\pi}d\theta p(\mathbf{r},t\,|\,\mathbf{r}_0)\\ &=\frac{1}{2\pi}\int_0^\infty dkk\tilde{p}(\mathbf{k},t)\left[\frac{1}{2\pi}\int_0^{2\pi}d\theta J_0(k\sqrt{r^2+r_0^2-2rr_0\cos\theta})\right]\\ &=\frac{1}{2\pi}\int_0^\infty dkk\tilde{p}(\mathbf{k},t)\left[J_0(kr)J_0(kr_0)\right] \end{aligned} \tag{S4-8}$$

To obtain the final equation in Eq. (S4-8), we have used the addition theorem for the Bessel function, $J_0(kR)$, i.e., $J_0(kR)=J_0(kr)J_0(kr_0)+2\sum_{n=1}^\infty J_n(kr)J_n(kr_0)\cos(n\theta)$.

The radially symmetric propagator, $p_1(r,t\,|\,r_0)$, satisfying the absorbing boundary condition, $p_1(\sigma,t\,|\,r_0)=0$, can be obtained by modifying the $(r,\,r_0)$-dependent factor within the square bracket in Eq. (S4-8). When the diffusion coefficient, *D*, does not undergo any stochastic fluctuation but is constant over time as $D=\langle D\rangle$, and $1-\tilde{f}(\mathbf{k})$ in Eq. (S3-28) is replaced by $k^2\langle l^2\rangle/4$ with $d=2$, the analytical expression of $\hat{p}_1(r,s\,|\,r_0)$ is given by (*42*)

$$\hat{p}_1(r,s\,|\,r_0)=\frac{1}{2\pi\langle D\rangle}K_0(\zeta r)K_0(\zeta r_0)\left[\frac{I_0(\zeta r_<)}{K_0(\zeta r_<)}-\frac{I_0(\zeta\sigma)}{K_0(\zeta\sigma)}\right] \tag{S4-9}$$

where $\zeta=\sqrt{s/\langle D\rangle}$ and $r_<=\min(r,r_0)$. In Eq. (S4-9), $I_\nu(z)$ and $K_\nu(z)$ respectively denote the νth-order modified Bessel functions of the first and the second kind. Using the Bromwich integral formula (*62*), the inverse Laplace transform of Eq. (S4-9) can be calculated as

$$p_1(r,t\,|\,r_0)=\frac{1}{2\pi}\int_0^\infty dkke^{-t\langle D\rangle k^2}\times\frac{\left[J_0(k\sigma)Y_0(kr)-J_0(kr)Y_0(k\sigma)\right]\left[J_0(k\sigma)Y_0(kr_0)-J_0(kr_0)Y_0(k\sigma)\right]}{J_0(k\sigma)^2+Y_0(k\sigma)^2} \tag{S4-10}$$

where $Y_\nu(z)$ denotes the νth-order Bessel function of the second kind. Equation (S4-10) tells us how the (r, r_0)-dependent factor in Eq. (S4-8) must be modified to make $p_1(r,t\,|\,r_0)$satisfy the absorbing boundary condition, $p_1(\sigma,t\,|\,r_0)=0$. When a random walker obeys the generalized transport equation, Eq. (S3-4), characterized by Eqs. (S3-24) and (S3-25) with $\lambda_i=\lambda=\tau^{-1}$, $p_1(r,t\,|\,r_0)$ reads as

$$p_1(r,t\,|\,r_0)=\frac{1}{2\pi}\int_0^\infty dkk\tilde{p}(\mathbf{k},t)\times\frac{\left[J_0(k\sigma)Y_0(kr)-J_0(kr)Y_0(k\sigma)\right]\left[J_0(k\sigma)Y_0(kr_0)-J_0(kr_0)Y_0(k\sigma)\right]}{J_0(k\sigma)^2+Y_0(k\sigma)^2} \tag{S4-11}$$

where $\tilde{p}(\mathbf{k},t)$ is given by Eq. (S3-28).

To calculate the survival probability, $S_1(t\,|\,r_0)$, associated with Eq. (S4-11), let us substitute Eq. (S4-11) into Eq. (S4-6) with $d=2$, resulting in

$$S_1(t\,|\,r_0)=\int_0^\infty dkk\tilde{p}(\mathbf{k},t)\frac{J_0(k\sigma)Y_0(kr_0)-J_0(kr_0)Y_0(k\sigma)}{J_0(k\sigma)^2+Y_0(k\sigma)^2}\times\int_\sigma^\infty drr\left[J_0(k\sigma)Y_0(kr)-J_0(kr)Y_0(k\sigma)\right] \tag{S4-12}$$

On the right-hand side of Eq. (S4-12), however, the numerical integration of $r\left[J_0(k\sigma)Y_0(kr)-J_0(kr)Y_0(k\sigma)\right]$ over r is not well-defined because for given k and σ, $r\left[J_0(k\sigma)Y_0(kr)-J_0(kr)Y_0(k\sigma)\right]$ oscillates over r in such a divergent manner that its amplitude keeps increasing with r. Note here that $p_1(r,t\,|\,r_0)$ obtained after the whole-k integration is a well-behaved function of r that satisfies the condition that $p_1(r,t\,|\,r_0)$ approaches zero in the large-r

limit. Introducing the exponentially decreasing function, e^{-sr} ($s > 0$), of r to solve the problem involved in the integration over r in Eq. (S4-12), Eq. (S4-12) can be rewritten as

$$S_1(t \mid r_0) = \int_0^\infty dk k \tilde{p}(\mathbf{k},t) \frac{J_0(k\sigma)Y_0(kr_0) - J_0(kr_0)Y_0(k\sigma)}{J_0(k\sigma)^2 + Y_0(k\sigma)^2} \times \left\{ -\lim_{s\to 0} \partial_s \int_\sigma^\infty dr e^{-sr} \left[J_0(k\sigma)Y_0(kr) - J_0(kr)Y_0(k\sigma) \right] \right\} \quad \text{(S4-13)}$$

After some manipulation with the Bessel functions in Eq. (S4-13), we finally have

$$S_1(t \mid r_0) = \frac{2}{\pi} \int_0^\infty dk \frac{J_0(k\sigma)Y_0(kr_0) - J_0(kr_0)Y_0(k\sigma)}{\left[J_0(k\sigma)^2 + Y_0(k\sigma)^2 \right] k} \tilde{p}(\mathbf{k},t) \quad \text{(S4-14)}$$

In Eq. (S4-14), we don't need to use the Padé approximant to $1 - \tilde{f}(\mathbf{k})$ determining the k-dependence of $\tilde{p}(\mathbf{k},t)$ unlike Eq. (S3-31) because for given σ and r_0, the k-dependent integrand itself in front of $\tilde{p}(\mathbf{k},t)$ gradually approaches zero in an oscillatory manner as k increases, assuring the convergence of the integration over k in Eq. (S4-14). When $1 - \tilde{f}(\mathbf{k})$ in Eq. (S3-28) is replaced by $k^2\langle l^2 \rangle / 2d$, the one- and three-dimensional formulas of $p_1(r,t \mid r_0)$ and $S_1(t \mid r_0)$ are presented in ref. (*60*).

Eq. (S4-11) or (S4-14) is applicable to the case where one nanoparticle moves with respect to the other nanoparticle pinned at the coordinate origin. For a pair of mobile nanoparitlces, the mean, $\langle D_r \rangle$, and the relative variance, $\eta_{D_r}^2$, of the relative diffusion coefficient, D_r, and the distribution, $f_r(l)$, of the relative jump length should be used instead of the mean, $\langle D \rangle$, and the relative variance, η_D^2, of the diffusion coefficient, D, and the distribution, $f(l)$, of the jump length. Values of relative diffusion coefficients are estimated from the linear time dependence of the time-averaged variance of the relative displacement, $\Delta\mathbf{r}_{12}(t;t_0)\left[= \mathbf{r}_{12}(t+t_0) - \mathbf{r}_{12}(t_0) \right]$, defined for a given pair of coalescing nanoparticles 1 and 2. Here, $\mathbf{r}_{12}$ denotes the relative position vector, $\mathbf{r}_{12} = \mathbf{r}_1 - \mathbf{r}_2$

, defined with $\mathbf{r}_1$ and $\mathbf{r}_2$ indicating the positions of the particles 1 and 2, respectively. In addition, like the distribution of the jump length, the distribution of the relative jump length can also be modelled as the exponential distribution, $f_r(l) = e^{-l/l_r}/2\pi l_r^2$ with l_r denoting the characteristic relative jump length as shown in Fig. S20. With $d = 2$, $a = n/2 = \eta_{D_r}^{-2}$, $b = \langle D_r \rangle \eta_{D_r}^2$, and the Fourier transform, $\tilde{f}_r(\mathbf{k})$, of $f_r(l)$, given by $\tilde{f}_r(\mathbf{k}) = (1 + k^2 l_r^2)^{-3/2}$, Eq. (S3-28) can then be rewritten as

$$\tilde{p}(\mathbf{k},t) = \left[\frac{4\mu_k e^{-(\mu_k - 1)t/\tau}}{(\mu_k + 1)^2 - (\mu_k - 1)^2 e^{-2\mu_k t/\tau}} \right]^{1/\eta_{D_r}^2}; \ \mu_k = \left(1 + \frac{8\langle D_r \rangle \eta_{D_r}^2 \tau}{\langle l^2 \rangle_r} [1 - \tilde{f}_r(\mathbf{k})] \right)^{1/2} \tag{S4-15}$$

where $\langle l^2 \rangle_r$ denotes the second-order moment of $f_r(l)$, calculated as $\langle l^2 \rangle_r = 6 l_r^2$. For a later use in Fig. S27, we also provide the diffusive transport version of Eq. (S4-15) as follows:

$$\tilde{p}(\mathbf{k},t) = \left[\frac{4\mu_k e^{-(\mu_k - 1)t/\tau}}{(\mu_k + 1)^2 - (\mu_k - 1)^2 e^{-2\mu_k t/\tau}} \right]^{1/\eta_{D_r}^2}; \ \mu_k = \left(1 + 2\langle D_r \rangle \eta_{D_r}^2 \tau k^2 \right)^{1/2} \tag{S4-16}$$

where $1 - \tilde{f}_r(\mathbf{k})$ in Eq. (S4-15) has been replaced by $k^2 \langle l^2 \rangle_r / 2d = k^2 \langle l^2 \rangle_r / 4$.

In the two-step coalescence scheme described in Fig. 5A of the main text, σ is defined as the contact separation upon a ligand-mediated contact between nanoparticles, i.e., the sum of the thickness of the double ligand layer, 1.4 nm, and the core-core contact distance, $\sigma_c (= r_1 + r_2)$, defined for a given pair of coalescing nanoparticles 1 and 2 with r_1 and r_2 denoting the core radii of the particles 1 and 2. Because σ_c varies from coalescing pair to coalescing pair, we need to consider the σ-averaged survival probability, $\langle S(t \mid r_0) \rangle_\sigma$, which is obtained by averaging both sides of Eq. (S4-5) over σ as

$$\langle S(t \mid r_0) \rangle_\sigma = e^{-kt} + k \int_0^t dt' e^{-k(t-t')} \langle S_1(t' \mid r_0) \rangle_\sigma \tag{S4-17}$$

where $S_1(t \mid r_0)$ is given by Eq. (S4-14) with Eq. (S4-15). In Fig. 5C of the main text, we presented the theoretical results obtained by calculating Eq. (S4-17) with the values of $\langle D_r \rangle$, $\eta_{D_r}^2$, and l_r given by $\langle D_r \rangle = 0.382$ nm^2/s, $\eta_{D_r}^2 = 0.375$, and $l_r = 0.196$ nm, respectively. The value of the diffusivity relaxation time, τ, which is one of intrinsic characteristics of the environment nanoparticles are embedded in, is chosen to be the same as determined in Fig. 2B in the main text.

For the single-step coalescence scheme where two nanoparticles initially distant by r_0 merge together upon a direct contact between their nanoparticle cores (Fig. 5A in the main text), we presented the theoretical results obtained by calculating $\left\langle S_1(t \mid r_0) \right\rangle_{\sigma_c}$ in Fig. 5C of the main text. Here, $\left\langle S_1(t \mid r_0) \right\rangle_{\sigma_c}$ is obtained by averaging $S_1(t \mid r_0)$ over the core-core contact distance, σ_c, where $S_1(t \mid r_0)$ is the same as used in the two-step coalescence scheme except that σ is replaced by σ_c, explicitly,

$$S_1(t \mid r_0) = \frac{2}{\pi} \int_0^\infty dk \, \frac{J_0(k\sigma_c) Y_0(kr_0) - J_0(kr_0) Y_0(k\sigma_c)}{\left[J_0(k\sigma_c)^2 + Y_0(k\sigma_c)^2 \right] k} \tilde{p}(\mathbf{k}, t) \tag{S4-18}$$

with $\tilde{p}(\mathbf{k}, t)$ being given by Eq. (S4-15).

Finally, we consider the survival probability, $S_T(t)$, accounting for coalescence events between nanoparticles located at various separations. $S_T(t)$ is equivalent to the ratio, $\rho_T(t) / \rho_T(t_0)$, between the number densities of nanoparticles at a time $t (\geq t_0)$ and the initial time, t_0. The nanoparticle number density, $\rho_T(t)$, satisfies the following rate equation:

$$\frac{\partial}{\partial t} \rho_T(t) = -k_f(t) \rho_T(t)^2, \tag{S4-19}$$

where $k_f(t)$ denotes the forward bimolecular coalescence rate coefficient, which is related to the fraction of nanoparticle pairs initially distant by r_0 that coalesce per unit time, or $-\partial_t S(t\,|\,r_0)$ by (*61*)

$$k_f(t) = -\int_{r_c}^{\infty} dr_0 \gamma_d r_0^{d-1} g(r_0) \partial_t S(t\,|\,r_0). \tag{S4-20}$$

In Eq. (S4-20), $g(r_0)$ and r_c denote the initial pair correlation function and the short-range cutoff distance, respectively. With Eq. (S4-17) and $d = 2$ at hand, the corresponding rate cofficient can be written from Eq. (S4-20) as

$$k_f(t) = -2\pi \int_{r_c}^{\infty} dr_0 r_0 g(r_0) \partial_t \left\langle S(t\,|\,r_0) \right\rangle_{\sigma}. \tag{S4-21}$$

Using Eq. (S4-19), the relation between $S_T(t)$ and $k_f(t)$, given by Eq. (S4-21), can be obtained as

$$S_T(t) = \frac{1}{1 + \int_0^t dt' k_f(t') \rho_T(t_0)}. \tag{S4-22}$$

Equation (S4-22) is used in Fig. S29 with Eqs. (S4-17) and (S4-21), the same parameter values as in Fig. 5C, and the initial pair correlation function being given by the short-time profile for the pair correlation function in Fig. 3D. The value of r_c is chosen as the sum of the mean nanoparticle diameter, 1.4 nm, and the thickness, 1.4 nm, of the double ligand layer formed upon nanoparticle contact.

S5. Rotational motion of nanoparticles

The rotational diffusion coefficient of nanoparticles can be measured by tracking rotational motion of the nanoparticles. Although it is difficult to quantify rotational motion of a nanoparticle in low-magnification TEM images for a spherical nanoparticle as observed in our experiments, the degree of the nanoparticle rotation can be estimated from changes in the lattice fringes of a crystalline nanoparticle in its time-series TEM images with a sufficient resolution (*59*).

In our observations, we could identify the changes in the lattice fringes of three gold nanoparticles, with diameters ranging from 2.5 nm to 4 nm. As shown in the snapshots of the *in situ* TEM movie of a representative nanoparticle, (Fig. S24A and movie S4), the lattice fringes of the nanoparticle rotate over time. The lattice fringes of the nanoparticle correspond to the (111) lattice plane of gold, and are visible when the crystallographic planes of the nanoparticle are nearly parallel to the viewing direction in TEM. The rotational motion of the rotating nanoparticles can be quantified by using the fast-Fourier transforms (FFTs) of the time-series TEM images. In Fig. S24B, the direction represented by the straight line joining two circles centered on a pair of peaks corresponds to Au [111] direction. The rotational motion of the nanoparticle can then be quantified by changes in the angle, ϕ, between the Au [111] direction of the nanoparticle and the horizontal line of the image during the observation.

The rotational diffusion coefficient, D_R, of the nanoparticles can be estimated by calculating the time-ensemble-averaged variance, $\langle\overline{\delta\Delta\phi^2}\rangle$, of the angular displacement. In our observations, $\langle\overline{\delta\Delta\phi^2}\rangle$ is linear in time lags, indicating that the rotational motion of the nanoparticles follows normal diffusion as shown in Fig. S24C. Based on the relation, $\langle\overline{\delta\Delta\phi^2}\rangle = 2D_R t$, the optimized value of the rotational diffusion coefficient is found to be 0.318

rad^2/s, which is in close agreement with the value, 0.265 rad^2/s, of the rotational diffusion coefficient, estimated from the mean encounter complex lifetime identified as rotational relaxation time in the main text. It is also shown in Fig. S24D that the angular displacement distribution of the nanoparticle is well explained by the Gaussian distribution with the value of D_R = 0.318 rad^2/s. These agreement indicates that the rotational relaxation of the nanoparticles forming an encounter complex determines the lifetime of the complex, one of critical factors in kinetics of two-step coalescence between ligand-passivated nanoparticles.

S6. Nanoparticle movement near the liquid-vapor interface in a GLC

One interesting question to ask here would be, "How the observed diffusion and the coalescence of nanoparticles change when a liquid-vapor interface is introduced near the nanoparticles?" To answer this, we tracked ten nanoparticles in the vicinity of a nanobubble, which is generated with a relatively-low electron dose rate (Materials and Methods, and movie S5) (*21*). The nanoparticles near the nanobubble clearly show directed motion due to its growth (Fig. S25A). Note that no coalescence event between nanoparticles was observed despite the high density of nanoparticles at the liquid-vapor interface. The oriented attachment and coalescence between nanoparticles cannot occur when nanoparticle rotation is suppressed. The hindered rotation of nanoparticle is directly observed as a truncated nanoparticle pinned at the interface maintains a similar projected morphology during observation (Fig. S25B).

The effect of the moving interface on nanoparticle transport can be understood by examining the mean and the variance of longitudinal or transverse displacements of nanoparticles in the direction parallel or perpendicular to the displacement vector joining the initial and the final positions (Figs. S25C and S25D). The mean longitudinal displacement, $\langle\overline{\Delta r_{\parallel}(t)}\rangle$, grows linearly with time at a rate of 0.58 nm/s (Fig. S25C, orange line), which is close to the measured growth rate of the nanobubble, 0.47 nm/s (Figs. S25E and S26). These similar values demonstrate that the growth of the nanobubble causes the ballistic motion of nanoparticles. On the other hand, the mean transverse displacement, $\langle\overline{\Delta r_{\perp}(t)}\rangle$, is essentially zero for all observation times (Fig. S25C, blue line), indicating that there is no directional bias in the transverse direction.

The degree of randomness in nanoparticle motion is reflected by the variance of nanoparticle displacements. The longitudinal diffusion coefficient, $\langle D_{\parallel}\rangle$, and the transverse diffusion coefficient, $\langle D_{\perp}\rangle$, estimated from the linear time dependence of variances of longitudinal

and transverse displacements have similar values (Fig. S25D). The value, 0.17 nm^2/s, is nearly the same as the value of the diffusion coefficient, 0.12 nm^2/s, measured from the bubble-free GLC (Fig. 2A). Therefore, the moving interface near nanoparticles causes a shift of the mean particle position but has little influence on the fluctuation around the mean position.

S7. Estimation of electron-beam induced heating of GLC

The electron beam might affect the nanoparticle motion in the GLC through the local heating of a specimen induced by the irradiation. Small volume of the liquid encapsulated in a GLC (usually less than one attoliter) and an electron fluency required for high-resolution imaging might increase the temperature of the medium where nanoparticles diffuse. In addition, the presence of nanobubbles, which can be considered as a poor thermal conductor, in the vicinity of gold nanoparticles can signify the electron-beam induced heating effects. We calculated the amount of temperature rise for 1) gold nanoparticles in the quiescent GLC (movie S1) and 2) gold nanoparticles in a GLC with nanobubbles (movie S5). To estimate the maximum temperature rise caused by the electron beam, all energy dissipated during when electrons pass through the specimen is assumed to be converted to heat. According to previous studies (*12*, *64*), the electron-beam induced temperature rise, ΔT, of a particle in a medium is given by

$$\Delta T = \frac{J_e}{4h}\frac{dE}{dX} + \Delta T_{medium} \tag{S7-1}$$

where J_e, h, and dE/dX respectively denote the dose rate, the heat transfer coefficient of the surrounding medium, and the energy loss of the electron passing through the particle, all in SI units. Here, the first term of the right-hand side represents the temperature rise of a particle induced by the irradiation and its dissipation to the surrounding medium, and the second term of the right-had side represents the temperature rise of the medium. The total energy loss of the electron, dE/dX, is expressed as the product of the energy dissipation over the unit length, dE/dx, and the mean particle size, r_p. When the electron passes through a gold nanoparticle, dE/dx is given by 0.261 eV/nm (*12*). In addition, ΔT_{medium} is given by (*64*)

$$\Delta T_{medium} = \frac{a^2}{\alpha_{th} C_p}\psi\left(\frac{1}{4} + \frac{1}{2}\ln\frac{L}{a}\right) \tag{S7-2}$$

where α_{th}, a, C_p, and L respectively denote the thermal diffusivity, the beam radius, the specific heat capacity, and the liquid thickness. ψ represents the power adsorbed by a matter and given by

$$\psi = \left(1 + \frac{L}{\lambda}\right) S J_e \tag{S7-3}$$

where λ and S respectively denote the electron inelastic mean free path in the medium and the stopping power of the medium for electrons. Substituting Eqs. (S7-2) and (S7-3) into Eq. (S7-1) yields the temperature rise of the particle due to the electron beam irradiation.

$$\Delta T = \frac{J_e}{4h}\frac{dE}{dx} r_p + \frac{a^2}{\alpha_{th} C_p}\left(1 + \frac{L}{\lambda}\right) S J_e \left(\frac{1}{4} + \frac{1}{2}\ln\frac{L}{a}\right) \tag{S7-4}$$

For 200 keV electrons passing through the water, the value of λ is estimated to be 320 nm by interpolating the values measured at 120 keV and 300 keV (*51*). The values of S, α_{th}, h_{water}, and C_p of water are respectively given by 4.4768×10^{-14} J·m^2/kg (*65*), 1.4×10^{-7} m^2/s, 10^3 W/m^2·K, and 4180 J/kg·K. In our experiment, a, L, r_p, and J_e are found to be about 30 nm, 10 nm, 0.7 nm, and 10^4 e$^-$/Å·s. Putting these values into Eq. (S7-4) yields the value of the temperature rise of the gold nanoparticle fully immersed in a water, ~7 K. This value is only 2 % of the room temperature, and expected to give little effects on the nanoparticle mobility when the nanoparticles are suspended in the quiescent GLC (movie S1).

The presence of gas bubbles near nanoparticles can increase the temperature rise induced by the electron beam due to the smaller heat transfer coefficient of the gaseous species. The gas bubble formed during liquid-phase TEM experiment is known to be hydrogen gas, but we here adopt properties of air for the calculations. For air, h_{air}, α_{th}, and C_p respectively amount to 10 W/m^2·K, 2.239×10^{-5} m^2/s, and 1000 J/kg·K. When 200 keV electrons pass through the air, the value of S is given by 3.9584×10^{-14} J·m^2/kg according to ref. (*65*). λ is calculated to be 1252 nm

(*66*). As a result of calculations, the temperature of the gold nanoparticles fully surrounded by air is expected to increase by ~700 K. Although the degree of the temperature rise of the nanoparticles in the gas is significantly high, it should be noted that the observed nanoparticles indeed contact to both the encapsulated water and the gas bubble (movie S5). In this case, the heat of the nanoparticles can be transferred to the water and the air and the overall heat transfer coefficient can be obtained by simply adding the heat transfer coefficients of the air and the water by assuming parallel heat transfer processes, $h_{overall} = h_{water} + h_{air} \approx h_{water} = 1000$ W/m^2·K. Therefore, it can be seen that the electron-beam induced heating would not be significant if the nanoparticles make contact with the liquid medium. Most of the heat generated by electron scattering would be dissipated through the liquid, and we believe that the electron-beam induced heating may not significantly influence the nanoparticle dynamics observed in this work.

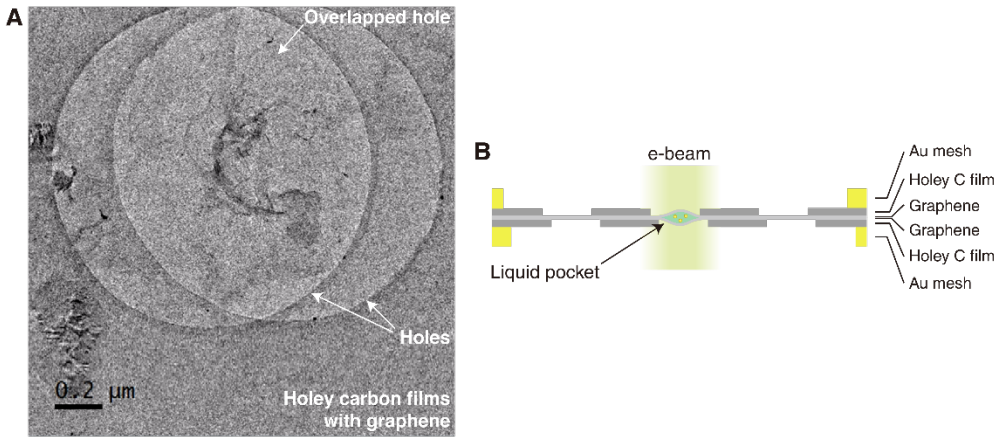

Fig. S1. Configuration of the graphene liquid cell. (**A**) TEM image showing liquid pocket within graphene liquid cell (GLC). In this image, the two holes of the carbon film TEM grids overlap. A sample liquid was encapsulated by two sheets of a suspended graphene in the overlapping region (Materials and Methods). (**B**) Schematic illustration of the side view showing the components of the GLC.

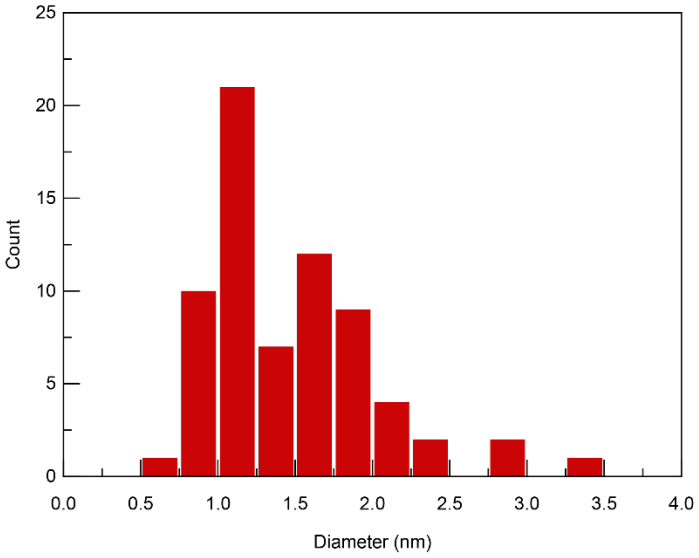

Fig. S2. Size distribution of nanoparticles. The diameters of 69 nanoparticles, measured directly from the *in situ* TEM movie (movie S1), range from 0.5 nm to 3.5 nm. The mean and the standard deviation of the nanoparticle diameters is calculated to be 1.47 nm and 0.52 nm, respectively.

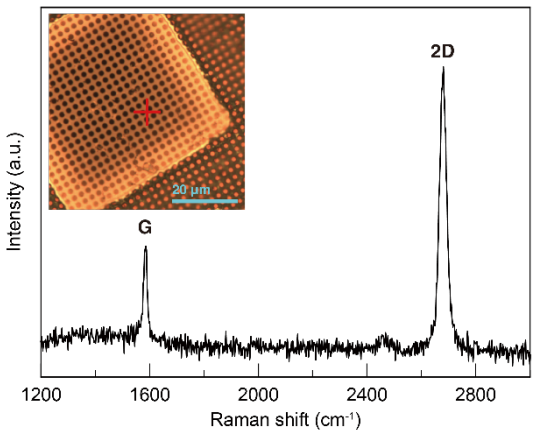

Fig. S3. Raman spectrum of graphene synthesized by chemical vapor deposition. Raman spectrum is obtained for a graphene sample transferred on a holey carbon TEM grid with an excitation wavelength of 532 nm. The negligible D band at 1350 cm^{-1} indicates that the graphene has few defects and hydrocarbon contaminations. (inset) Optical micrograph of the graphene-transferred TEM grid.

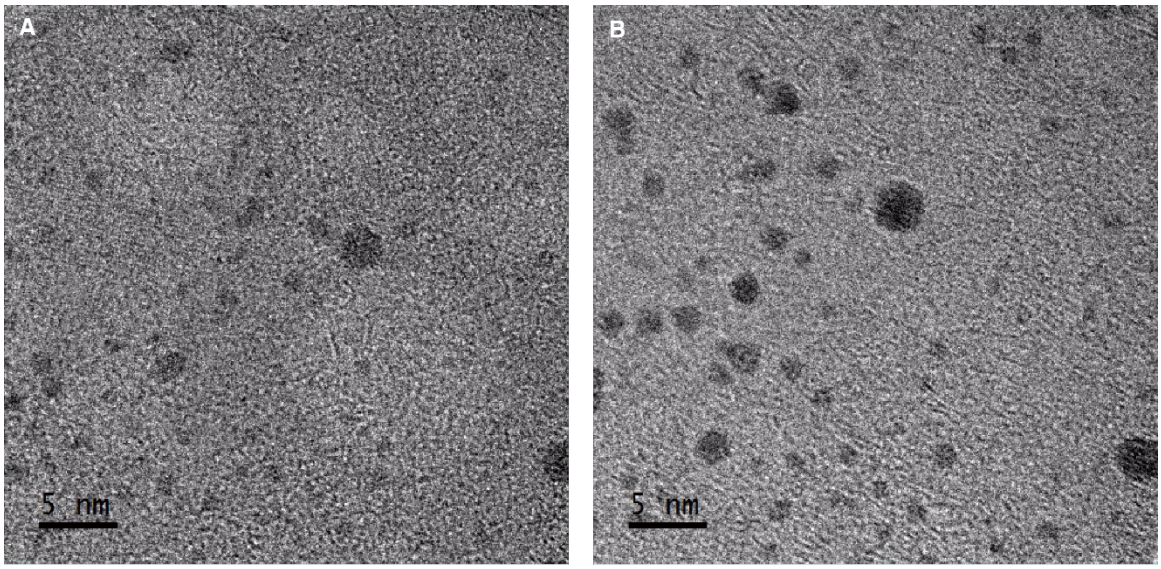

Fig. S4. Formation and disappearance of nanobubbles in the GLC. (**A**) TEM image showing the formation of nanobubbles at an early stage of the *in situ* TEM observation, confirming the presence of an entrapped liquid in the GLC. (**B**) TEM image obtained after nanobubbles disappeared under a more intense electron beam irradiation than in (A). The images shown in (A) and (B) were obtained in the same spatial region, and the time interval between (A) and (B) is 5.47 s.

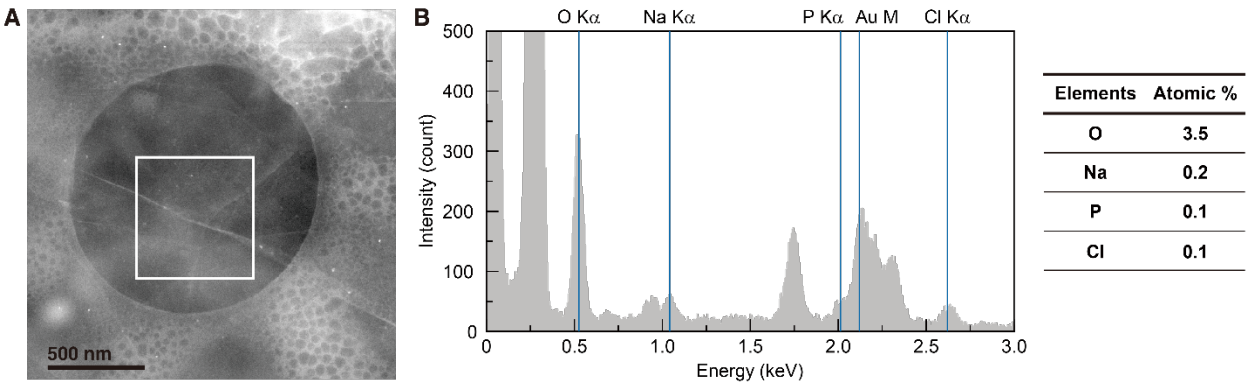

Elements	Atomic %
O	3.5
Na	0.2
P	0.1
Cl	0.1

Fig. S5. Energy-dispersive X-ray spectroscopy of GLC. (**A**) Annular dark-field scanning TEM image of GLC. (white box) The region where energy-dispersive X-ray spectroscopy (EDX) is performed. The presence of liquid is confirmed by observing bubble formation in TEM mode prior to the scanning TEM imaging. (**B**) EDX spectrum obtained in the region marked with the white box in (A). (table) Quantification result of the EDX spectrum. The oxygen Kα peak indicates the presence of water within the GLC. The atomic ratio of sodium to oxygen is 0.057, which is below the solubility, 0.11 in atomic ratio, of NaCl in water.

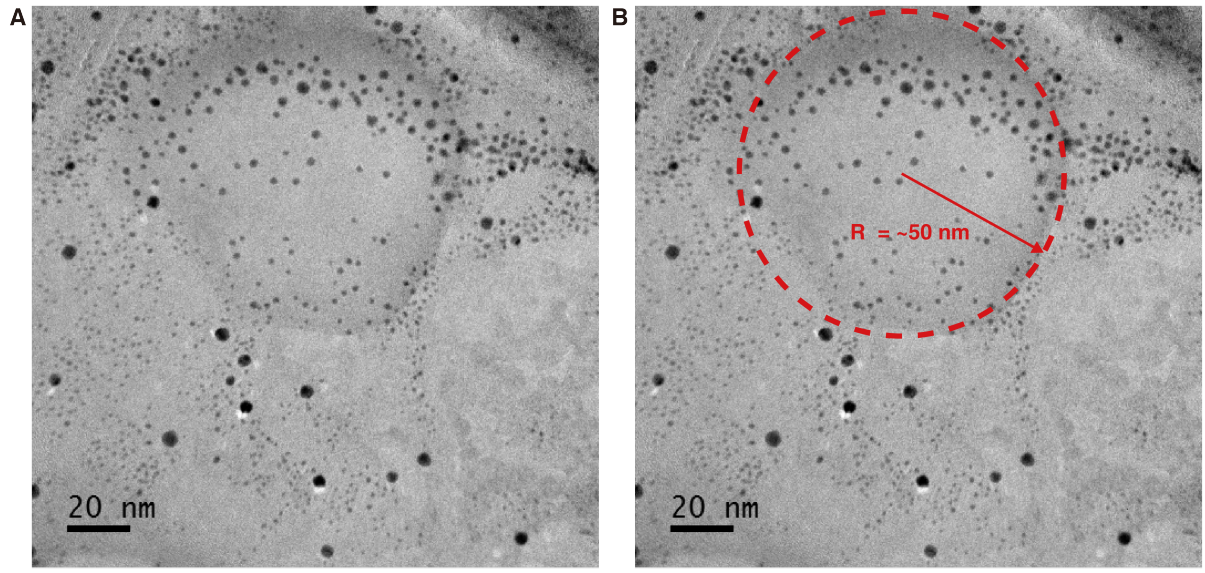

Fig. S6. The shape and the size of the liquid pocket within the GLC. (**A**) Raw TEM image of the liquid pocket, which was obtained by magnifying the center region of Fig. S1A. (**B**) TEM image shown in an overlaid by a circle to mark the boundary of the liquid pocket. The liquid pocket within the GLC has a blister-like shape with a radius of approximately 50 nm. The thickness of the liquid pocket is also estimated to be approximately 10 nm using the relationship between the radius and the thickness of the GLC reported in ref. (*28*). Note that the image was acquired from the *in situ* TEM observation for over three minutes in the center region of the GLC, which resulted in severe degradation of the GLC. The analysis described in the main text was performed over the first 18 seconds of the entire movie to circumvent the effects of GLC degradation on nanoparticle motion (Materials and Method).

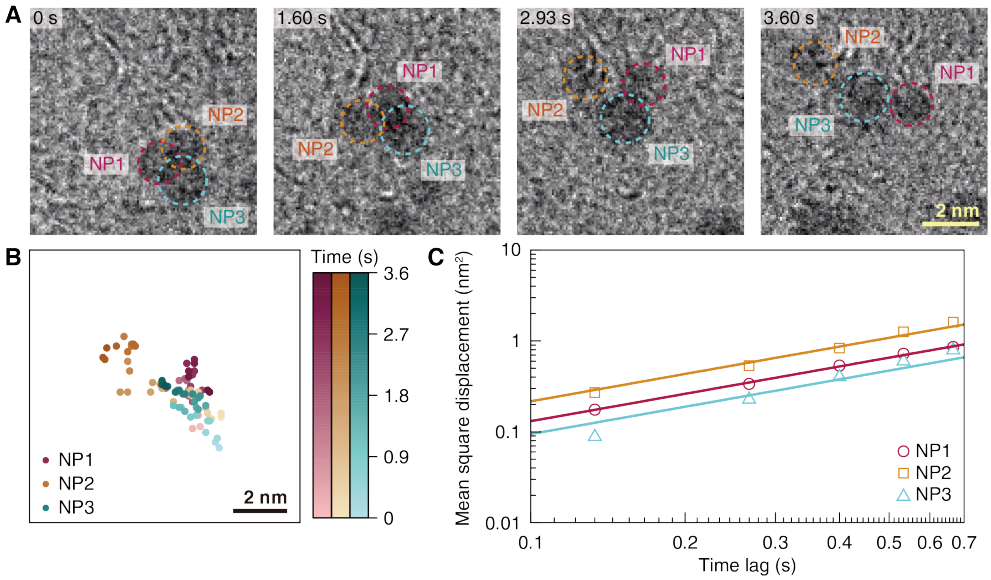

Fig. S7. Overlap event of three nanoparticles in GLC. (**A**) Time-series TEM images of the three nanoparticles, NP1, NP2, and NP3, which stay overlapped for a few seconds without coalescence between them. This overlap event indicates that the nanoparticles are located at different distances from the graphene surface (see section S1). (**B**) Trajectories of the three nanoparticles shown in (A). (**C**) Mean square displacements of the three nanoparticles shown in (A). The nanoparticle diffusivity varies slightly from nanoparticle to nanoparticle, presumably depending on the distance of the nanoparticle from the graphene surface.

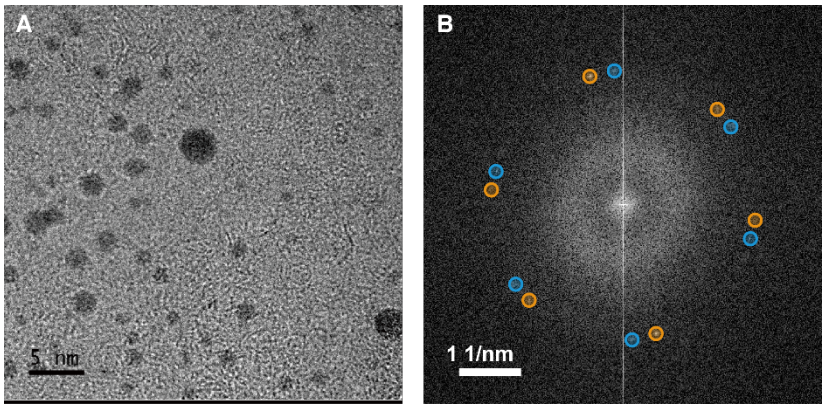

Fig. S8. Fast Fourier transform of a snapshot of the real-time TEM movie showing the presence of two graphene sheets. (**A**) Snapshot of the *in situ* TEM movie (movie S1). (**B**) Fast Fourier transform of the TEM image shown in (A), clearly showing two hexagonal patterns marked by orange and blue circles. Each hexagon indicates the presence of a single graphene sheet (see section S1 for more details).

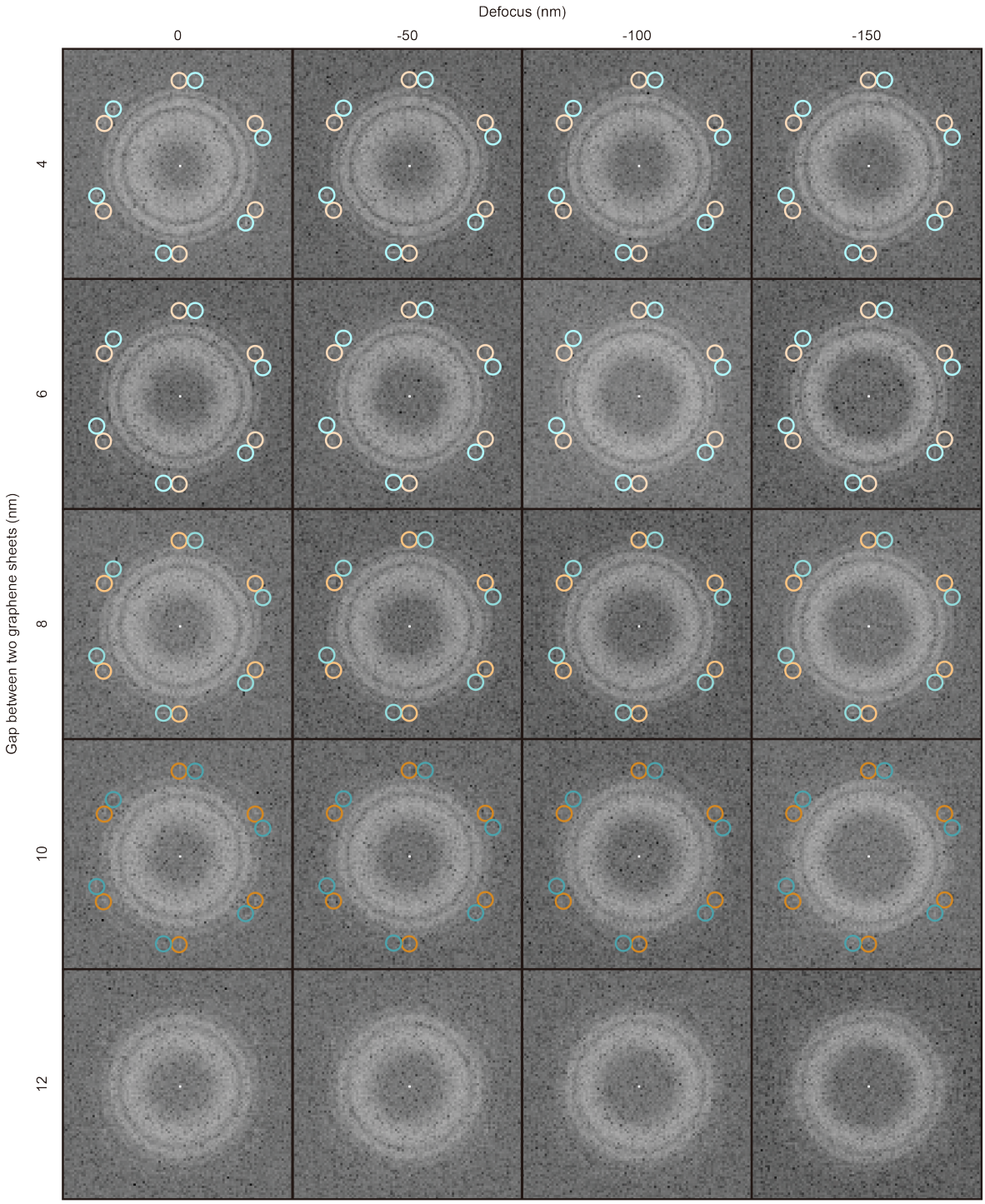

Fig. S9. Fast Fourier transforms of simulated TEM images of model GLCs with various values of thickness and defocus. Model GLCs consisting of TIP3P water molecules between two graphene sheets were simulated using the Large-scale Atomic/Molecular Massively Parallel

Simulator package. Trajectories of all atoms in model GLCs can be converted into TEM images using the multislice algorithm (see section S1 for details). Fast Fourier transforms of the simulated TEM images clearly show a bihexagonal pattern like Fig. S8B when the vertical distance, *d*, between the two sheets is small, while the bihexagonal pattern becomes gradually blurred and finally disappear as *d* increases.

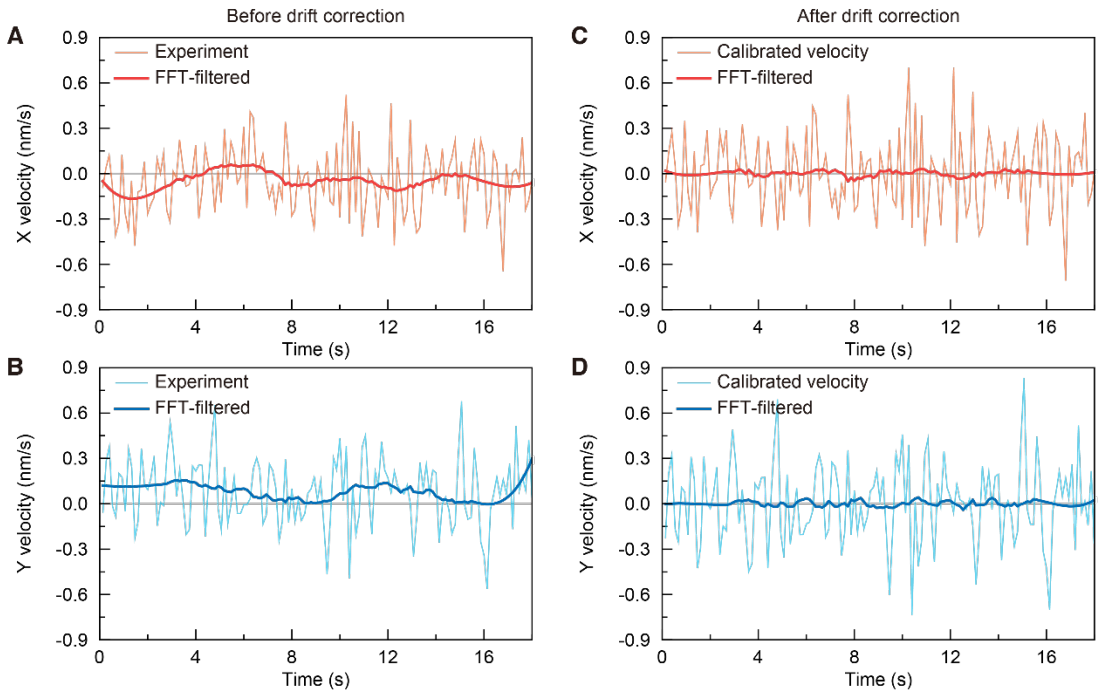

Fig. S10. Calibration of TEM specimen stage movement. (**A** and **B**) Mean nanoparticle velocities in the (**A**) *x*-direction and (**B**) *y*-direction in the *in situ* TEM images. (lines) Experimental data. (bold lines) Smoothed profiles of mean nanoparticle velocities using the fast Fourier transform (FFT) filter method in MATLAB. (**C** and **D**) Mean nanoparticle velocities in the (**C**) *x*-direction and (**D**) *y*-direction after calibration (see section S2 for details). (lines) Experimental data after calibration. (bold lines) Smoothed profiles of mean nanoparticle velocities after calibration.

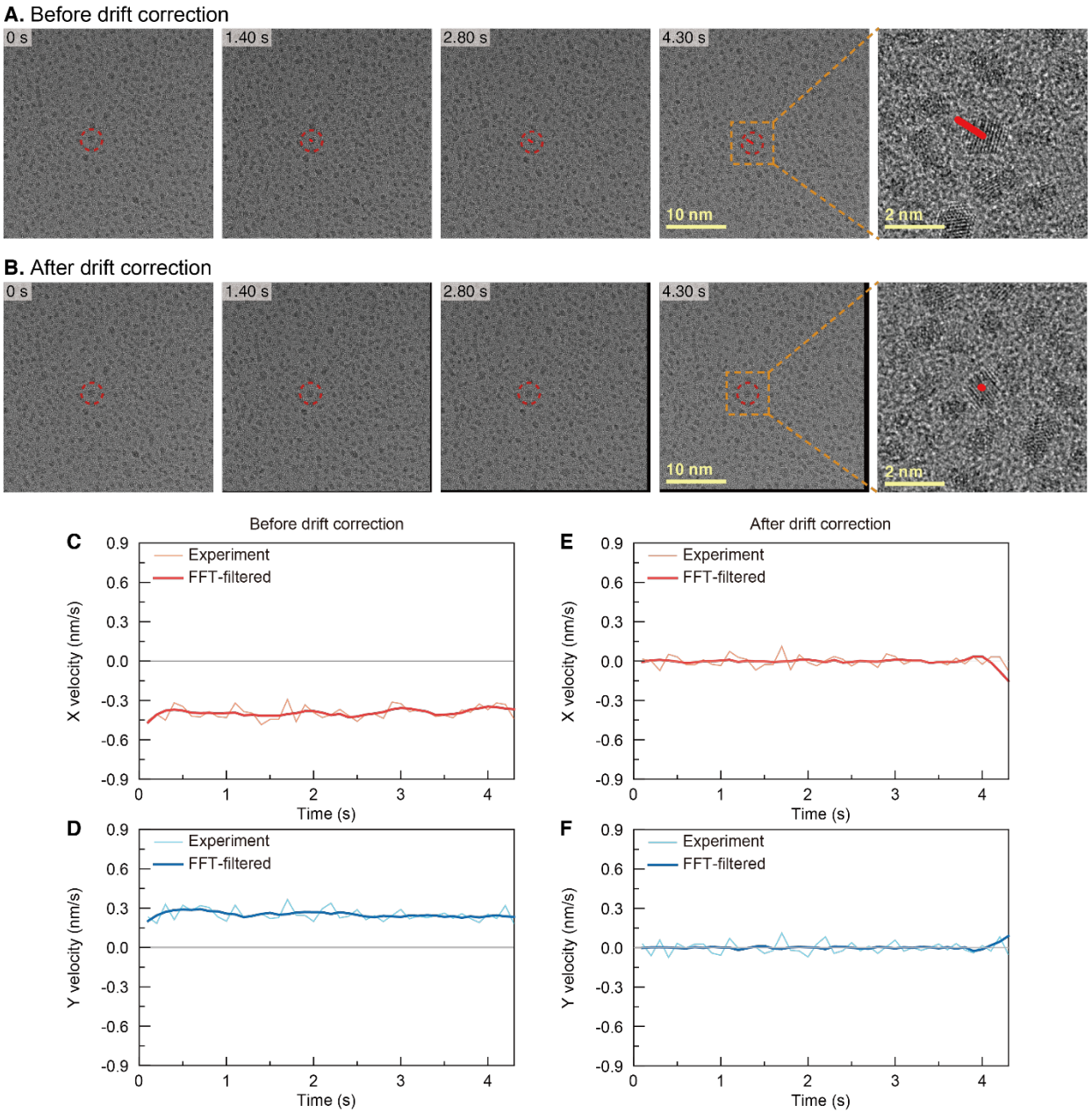

Fig. S11. Validation of our method for TEM specimen stage drift correction. (**A**) Time-series TEM images of gold nanoparticles dried on the graphene substrate moving in the direction of the TEM specimen stage drift. (dashed circle) Representative nanoparticle overlaid with its trajectory. In the rightmost panel, it is shown that the nanoparticle moves along the straight line parallel to the drift direction. (**B**) Time-series TEM images of gold nanoparticles after drift correction. (dashed circles) The nanoparticle marked in (A). In the rightmost panel, it is shown that the

nanoparticle's position after the drift correction does not change over time. (**C** and **D**) Mean nanoparticle velocities in the (**C**) *x*-direction and (**D**) *y*-direction in the *in situ* TEM images. (lines) Experimental data. (bold lines) Smoothed profiles of mean nanoparticle velocities using the fast Fourier transform (FFT) filter method in MATLAB. (**E** and **F**) Mean nanoparticle velocities in the (**E**) *x*-direction and (**F**) *y*-direction after calibration (see section S2 for details). (lines) Experimental data after drift correction. (bold lines) Smoothed profiles of mean nanoparticle velocities after drift correction.

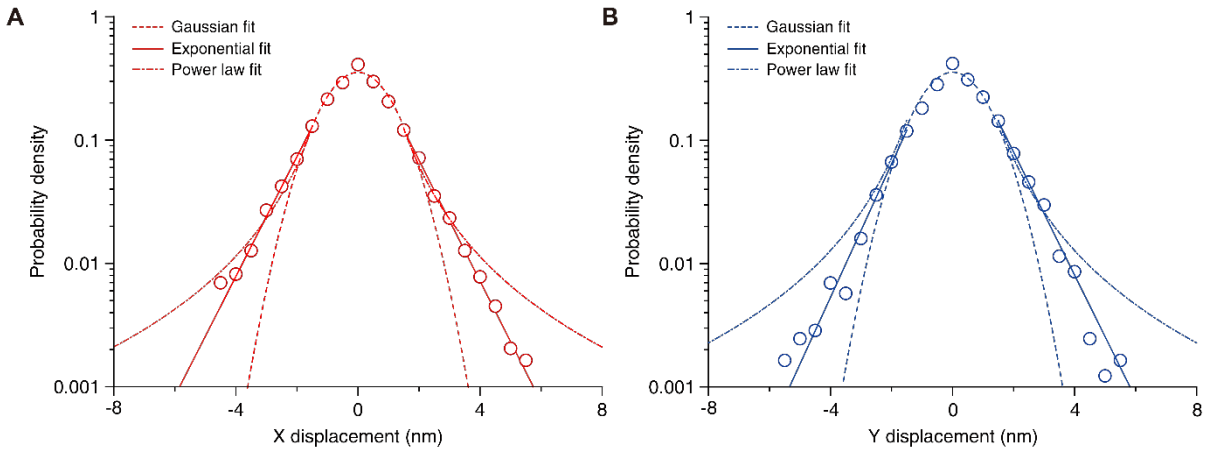

Fig. S12. Distribution of nanoparticle displacements during the experimental time resolution. Nanoparticle displacements in the (**A**) *x*-direction and (**B**) *y*-direction in the *in situ* TEM images during the temporal resolution. (symbols) Experimental data. (dashed lines) Gaussian fits best fitted to the central regions of the experimental data. (solid lines) Exponential fits best fitted to the tail regions of the experimental data. (dot-dashed lines) Power-law fits best fitted to the tail regions of the experimental data. As shown in the figure above, nanoparticle displacements are distributed as a single-peaked, unimodal distribution. Here, we could not detect any multimodal features (*12*) or any power-law characteristics of the displacement distributions caused by the large step movements (*10, 15*).

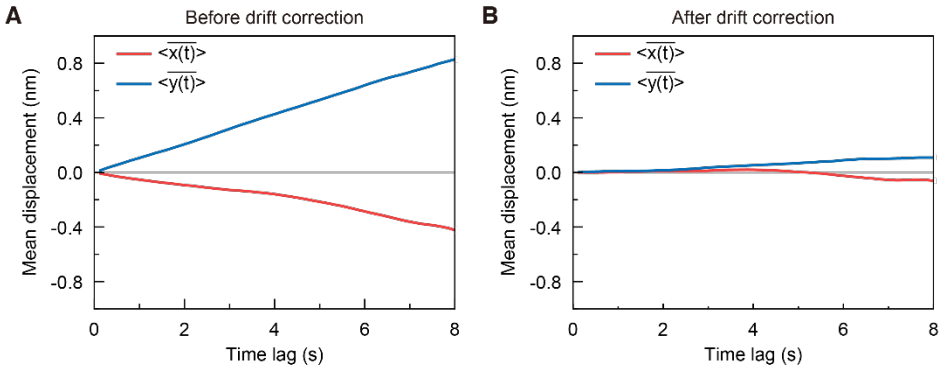

Fig. S13. Mean nanoparticle displacements. (**A** and **B**) Mean nanoparticle displacements (**A**) before drift calibration and (**B**) after drift calibration. (lines) Mean nanoparticle displacements in the *x*-direction and in the *y*-direction. The mean displacements become close to zero as a result of drift calibration (see section S2 for details), but the mean displacements after calibration still show finite values at long times. In order to account for the bias-free fluctuation in nanoparticle displacements, we used the difference, $\delta\Delta\mathbf{r}_i(t) = \left[\Delta\mathbf{r}_i(t) - \langle\overline{\Delta\mathbf{r}(t)}\rangle\right]$, between nanoparticle displacement and mean nanoparticle displacement in calculations of the variance of nanoparticle displacement and the non-Gaussian parameter.

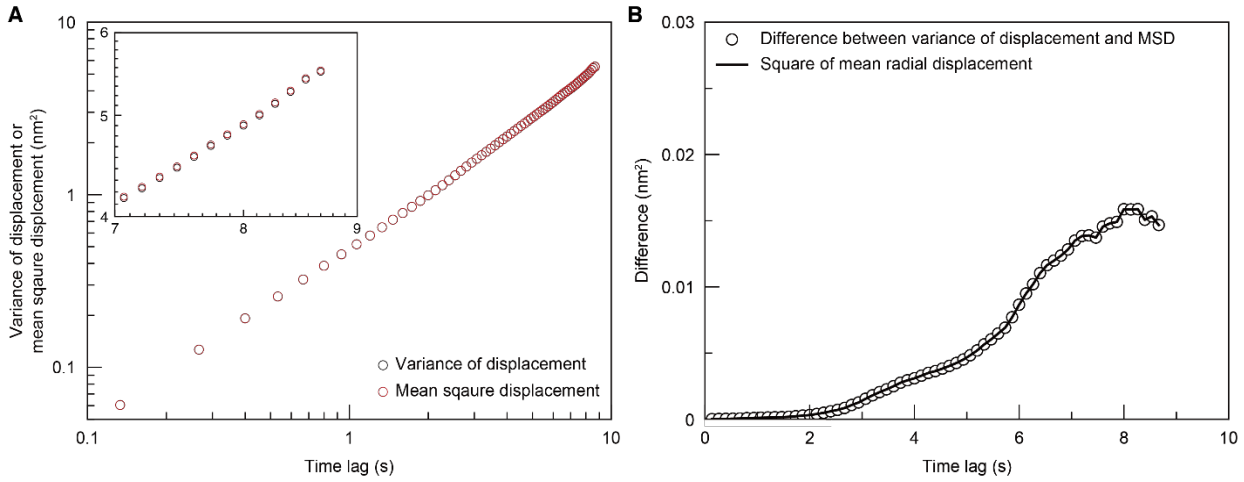

Fig. S14. Variance and mean square of nanoparticle displacements. (**A**) Variance of nanoparticle displacements (black symbols) and mean square displacement (MSD) (red symbols) of the nanoparticles. (**B**) The difference between the variance of nanoparticle displacements and the MSD (symbols). (line) Square of the mean displacement, $\langle \overline{\Delta \mathbf{r}(t)} \rangle$. The square of the mean displacement is the same as the difference between the variance of nanoparticle displacements and the MSD, indicating that the MSD includes the contribution from the nonzero mean displacement. In order to account for the fluctuation in nanoparticle displacements free of bias from the nonzero mean displacement, we consider the central moments of the nanoparticle displacement (see section S2).

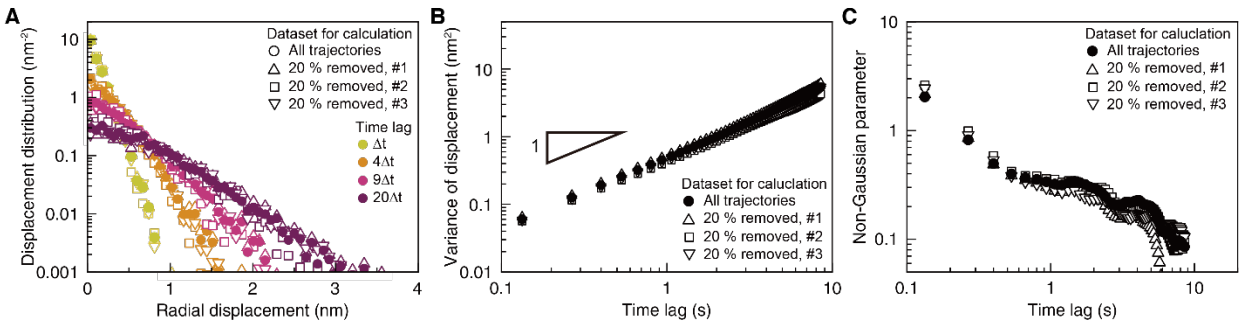

Fig. S15. Displacement distribution and related quantities measured for 20% less gold nanoparticles in the graphene liquid cell. (**A**) Distributions of nanoparticle displacements at various times. (filled symbols) Experimental data shown in Fig. 2E in the main text. (open symbols) Displacement distribution calculated after the random exclusion of 20 % of the nanoparticle trajectories used in Fig. 2E. (**B**) Time-ensemble-averaged variance of nanoparticle displacements. (filled symbols) Experimental data shown in Fig. 2A in the main text. (open symbols) Variance of displacement calculated after the random exclusion of 20 % of the nanoparticle trajectories. (**C**) Non-Gaussian parameter of the nanoparticle displacement. (filled symbols) Experimental data shown in Fig. 2B in the main text. (open symbols) Non-Gaussian parameter calculated after the random exclusion of 20 % of the nanoparticle trajectories. The nanoparticle displacement distributions, the variances of nanoparticle displacements, and the non-Gaussian parameters, calculated using the subset of the nanoparticle trajectories deviate only slightly from those calculated using the full nanoparticle trajectories.

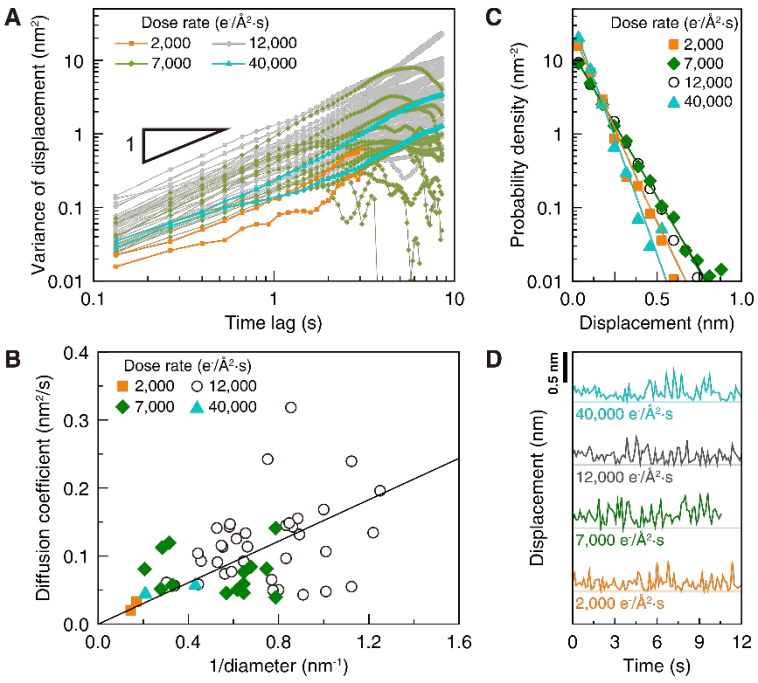

Fig. S16. Transport dynamics investigated under various electron dose rate conditions. (**A**) Single-particle time-averaged variance of nanoparticle displacements observed at different dose rates: (orange) about 2,000 $e^-/Å^2 \cdot s$, (green) 6,000 ~ 8,000 $e^-/Å^2 \cdot s$, or about 7,000 $e^-/Å^2 \cdot s$ for convenience (section S6 and movie S5), (grey) 10,000 ~ 14,000 $e^-/Å^2 \cdot s$, or about 12,000 $e^-/Å^2 \cdot s$ for convenience (movie S1), and (blue) about 40,000 $e^-/Å^2 \cdot s$. The nanoparticles follow Fickian diffusion in the range of the electron dose rates investigated. (**B**) Inverse size dependence of diffusion coefficient of nanoparticles observed at different dose rates. (line) Stokes-Einstein relation shown in Fig. 2D in the main text. The diffusion coefficient shows a positive correlation with the inverse nanoparticle diameter, while the positive correlation is not as strong as the ideal Stokes-Einstein relation. (**C**) Distributions of jump lengths of nanoparticles observed at different dose rates. (lines) Exponential distributions best fitted to the experimental data. (**D**) Time profiles of displacements of similar sized nanoparticles during the experimental time resolution at different dose rates. The time profiles of the nanoparticle displacement show similar behavior in the range of the dose rates investigated.

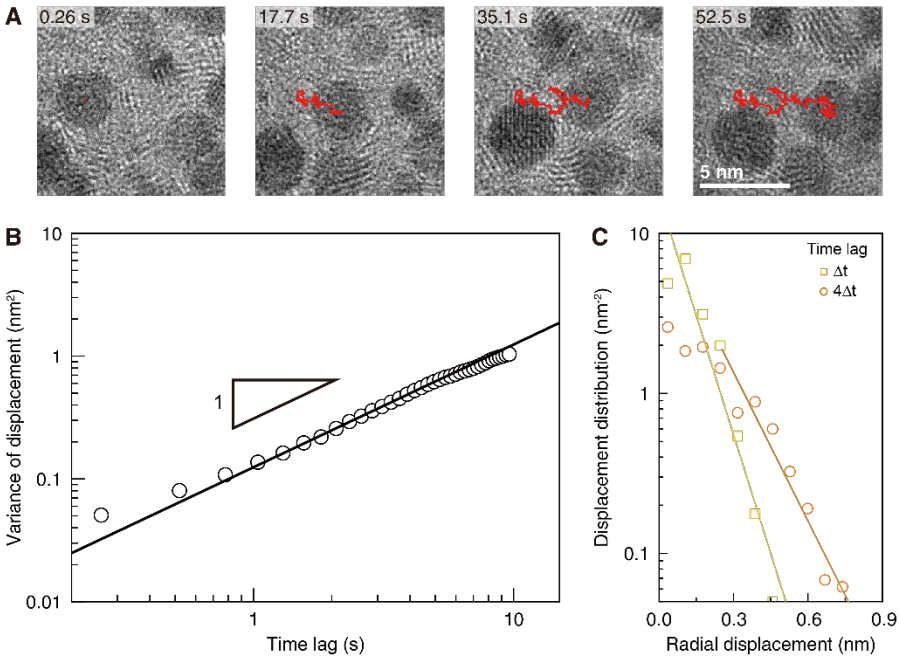

Fig. S17. Motion of oleylamine-passivated Pt nanoparticles suspended in *o*-dichlorobenzene solvent. (**A**) Snapshots of the *in situ* TEM movie of the Pt nanoparticles in a GLC (movie S2). (red lines) Trajectory of a represenatative nanoparticle with a diameter of 3.4 nm. The *in situ* TEM movie was captured for 52.26 seconds with a temporal resolution, Δt, of 0.26 seconds using the TEAM 1 microscope operated at 80 kV at the National Center for Electron Microscopy. (**B**) Variance of nanoparticle displacements of the nanoparticle marked in (A). (symbols) Experimental data. (black line) The best fit by $4\langle D\rangle t$. $\langle D\rangle$ is optimized to be 0.073 nm^2/s. (**C**) Distributions of nanoparticle displacements at various times. (symbols) Experimental data. (lines) Exponential tails of the displacement distributions.

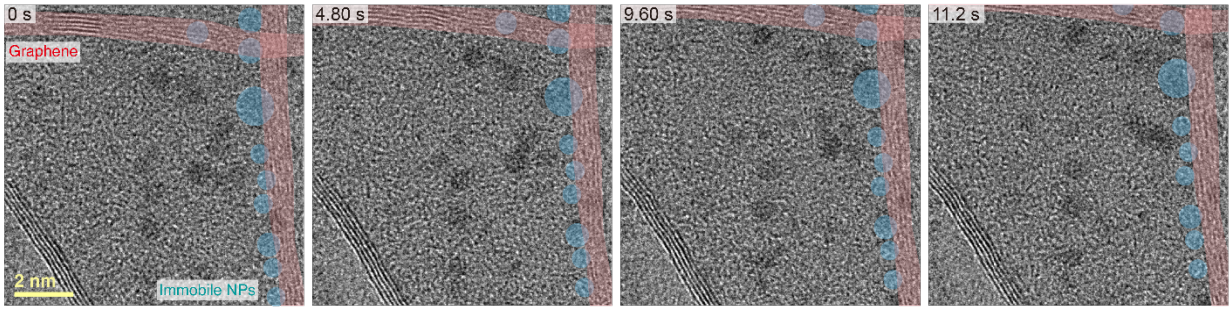

Fig. S18. Nanoparticles in graphene scroll. Time-series TEM images showing the nanoparticle motion in the liquid encapsulated within a graphene scroll were captured from movie S3 recorded under the same experimental condition as described in Materials and Methods and at the electron dose rate of about 10,000 ~ 14,000 $e^-/Å^2 \cdot s$. The graphene scroll containing the sample solution is formed as the graphene is unexpectedly rolled up during the GLC fabrication process. (0002) lattice planes of a multilayer graphene are visible, showing the side view of the graphene sheet, and marked with red color. As shown in movie S3, the nanoparticles located very close to the graphene surface, marked with blue color, do not show any noticeable movements, while the nanoparticles moving vigorously are away from the graphene surface. In combination with the overlapping event of three nanoparticles in the GLC (Fig. S7), our observation of the graphene scroll would suggest that most of the nanoparticles observed in movie S1 diffuse in the liquid, rather than on the graphene surfaces.

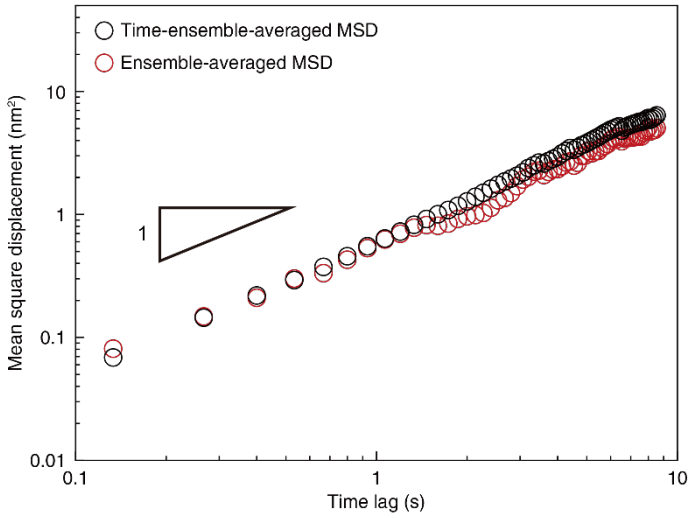

Fig. S19. Equivalence between the time-ensemble-averaged mean square displacement and the ensemble-averaged mean square displacement of nanoparticles. (black symbols) Time-ensemble-averaged mean square displacement (MSD) of the nanoparticles. (red symbols) Ensemble-averaged MSD of the nanoparticles. Both the time-ensemble-averaged MSD and the ensemble-averaged MSD linearly increase with time, and are the same as each other, indicating the ergodic behavior of the nanoparticles in the GLC.

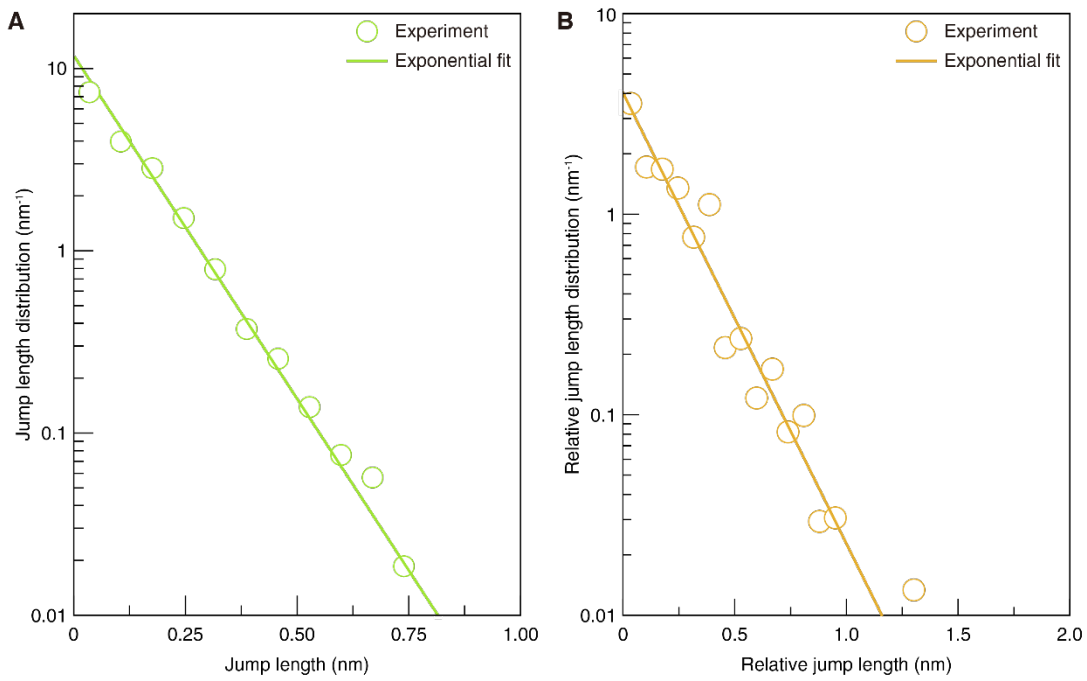

Fig. S20. Distributions of jump lengths and relative jump lengths of nanoparticles. (**A**) Distribution of jump lengths of nanoparticles. (symbols) Experimental data. (line) Exponential distribution, $f(l) \sim e^{-l/l_c}$, with parameters fit to experimental data. The value of the characteristic length, l_c, is found to be 0.10 nm, close to the value of l_c, 0.09 nm, obtained from the optimization of non-Gaussian parameter (section S3, see also Fig. 2B in the main text). (**B**) Distribution of relative jump lengths of coalescing nanoparticles. (symbols) Experimental data obtained from relative displacements of nanoparticles before the formation of transient nanoparticle complexes. (line) Exponential distribution, $f_r(l) \sim e^{-l/l_r}$, fit to the experimental data with the value of the characteristic length, l_r, given by 0.196 nm (section S4). The optimized exponential distributions in (A) and (B) are in good agreement with the experimental data, i.e., the distributions of displacements and relative displacements at $t = \Delta t$, respectively.

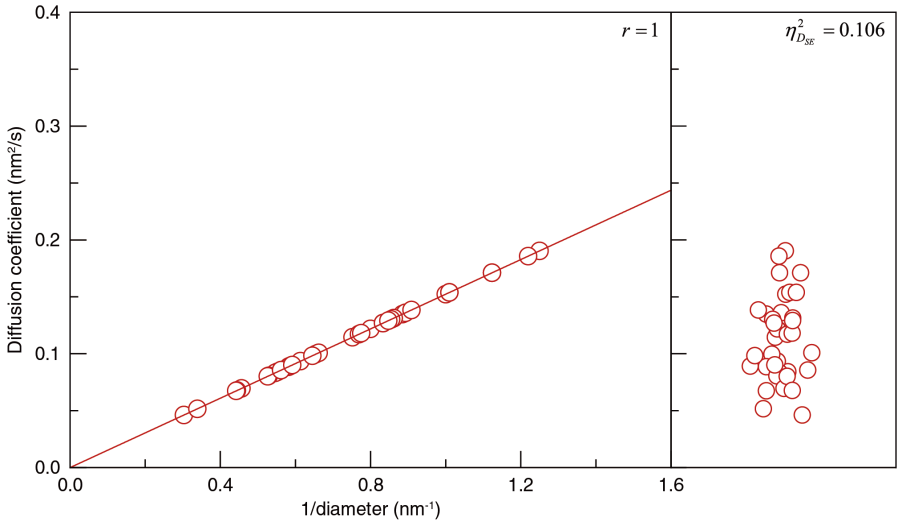

Fig. S21. Hypothetical diffusion coefficients of nanoparticles estimated by using the Stokes-Einstein relation. Hypothetical diffusion coefficients of nanoparticles estimated under the assumption that the nanoparticles perfectly follow the Stokes-Einstein relation. They are calculated by inserting measured nanoparticle sizes into the Stokes-Einstein relation with the effective viscosity identified by the best fit in Fig. 2D in the main text. The mean and the relative variance of the hypothetical diffusion coefficient are calculated as 0.113 nm^2/s and 0.106, respectively. The mean of the hypothetical diffusion coefficient is nearly the same as the observed mean diffusion coefficient, 0.12 nm^2/s, but the relative variance of the hypothetical diffusion coefficient is smaller than the observed relative variance, 0.26, indicating that the observed heterogeneity in nanoparticle diffusivity does not result solely from the heterogeneity in nanoparticle size.

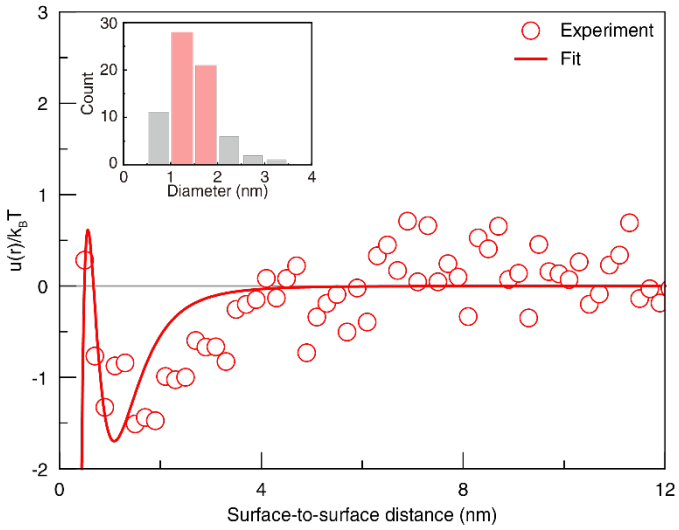

Fig. S22. Potential of mean force between nanoparticles. (symbols) Potential of mean force calculated from the experimental pair correlation function, $\rho(r_{surf},t)$. (inset) Histogram of nanoparticle diameters. $\rho(r_{surf},t)$ is obtained from surface-to-surface distances, r_{surf}, of nanoparticles tracked when the number of nanoparticles does not change for one second after beginning observation. In addition, only nanoparticles with diameters between 1 nm and 2 nm (colored bins in the inset) were chosen to account for the potential of mean force between similar sizes of nanoparticles. (line) Best fit of the model for the potential of mean force (*55*):

$$U(r_{surf}) = W_0 e^{-r_{surf}/\lambda} - \frac{A}{6}\left[\frac{2R^2}{(4R+r_{surf})r_{surf}} + \frac{2R^2}{(2R+r_{surf})^2} + \ln\frac{(4R+r_{surf})r_{surf}}{(2R+r_{surf})^2}\right]$$

On the right-hand side of the above equation, the first and second terms respectively represent the hydration repulsive potential and the van der Waals attractive potential with A and R denoting the Hamaker constant and the nanoparticle radius. Here, the value of R is 1.44 nm, the mean radius of the nanoparticles in question. The optimized values of the adjustable parameters are given by $W_0 = 1.15\times10^{-18}$ J, $A = 8.42\times10^{-18}$ J, and $\lambda = 0.23$ nm. Using the relationship between the hydration decay length, λ, and the ligand length, L_{ligand}, which is given by $L_{\text{ligand}} = \pi\lambda$ (*55*), the

length of the tris(4-*N*-methylcarbamoylphenyl)phosphine ligand used in this work is estimates as 0.72 nm (*19*). This value is consistent with the thickness, 1.4 nm, of the double ligand layer estimated from the surface-to-surface distance upon formation of transient nanoparticle complexes (see Fig. 4B in the main text and Fig. S23).

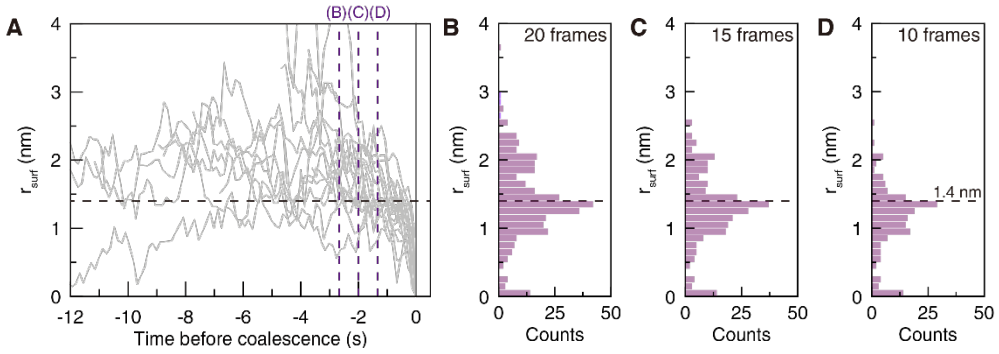

Fig. S23. Surface-to-surface distances between coalescing nanoparticles. (**A**) Changes of surface-to-surface distances, r_{surf}, of 20 coalescing nanoparticle pairs over time (Fig. 4B in the main text). (**B** to **D**), Histograms of r_{surf} calculated using (**B**) 20 frames, (**C**) 15 frames, and (**D**) 10 frames before coalescence. The histograms show a left-skewed peak around $r_{surf} = 1.4$ nm. This result indicates that a pair of nanoparticles form a transiently stable complex around $r_{surf} = 1.4$ nm, the distance where the potential of mean force attains its minimum value (see Fig. S22), and then coalesce.

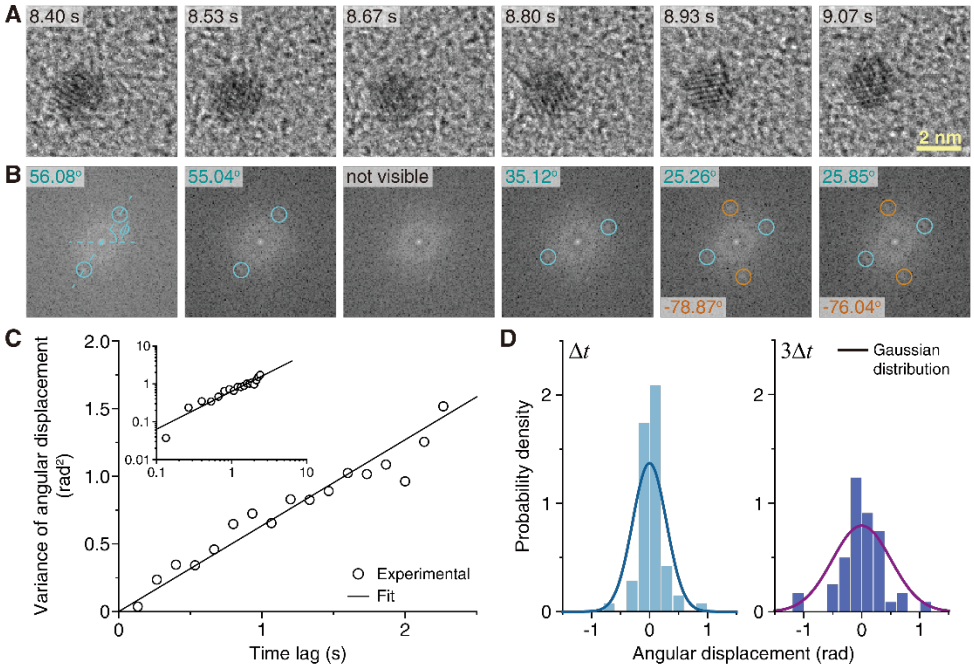

Fig. S24. Rotational motion of ligand-passivated gold nanoparticles in the graphene liquid cell. (**A**) Time-series TEM images, showing rotational motion of a representative nanoparticle identified with time-dependent changes in Au (111) lattice fringes (movie S4). (**B**) Fast-Fourier transforms (FFTs) of the TEM images in (A). ϕ represents the angle between the straight line joining two circles centered on a pair of peaks and the horizontal line (see section S5). (**C**) Time-ensemble-averaged variance, $\langle \overline{\delta\Delta\phi^2} \rangle$, of the angular displacement for three nanoparticles showing clear lattice fringes. (symbols) Experimental data. (line) The best fit by $2D_R t$. (inset) Double logarithmic plot. The optimized value of the rotational diffusion coefficient, D_R, is found to be 0.318 rad^2/s, which is in close agreement with the value of D_R estimated from the mean encounter complex lifetime identified as rotational relaxation time in the main text. (**D**) Distributions of angular displacements, $\Delta\phi$ during the temporal resolution Δt (left) and $3\Delta t$ (right). (histograms) Experimental data. (lines) Gaussian distributions with zero mean and the variance, $\langle \overline{\delta\Delta\phi^2} \rangle = 2D_R t$

.

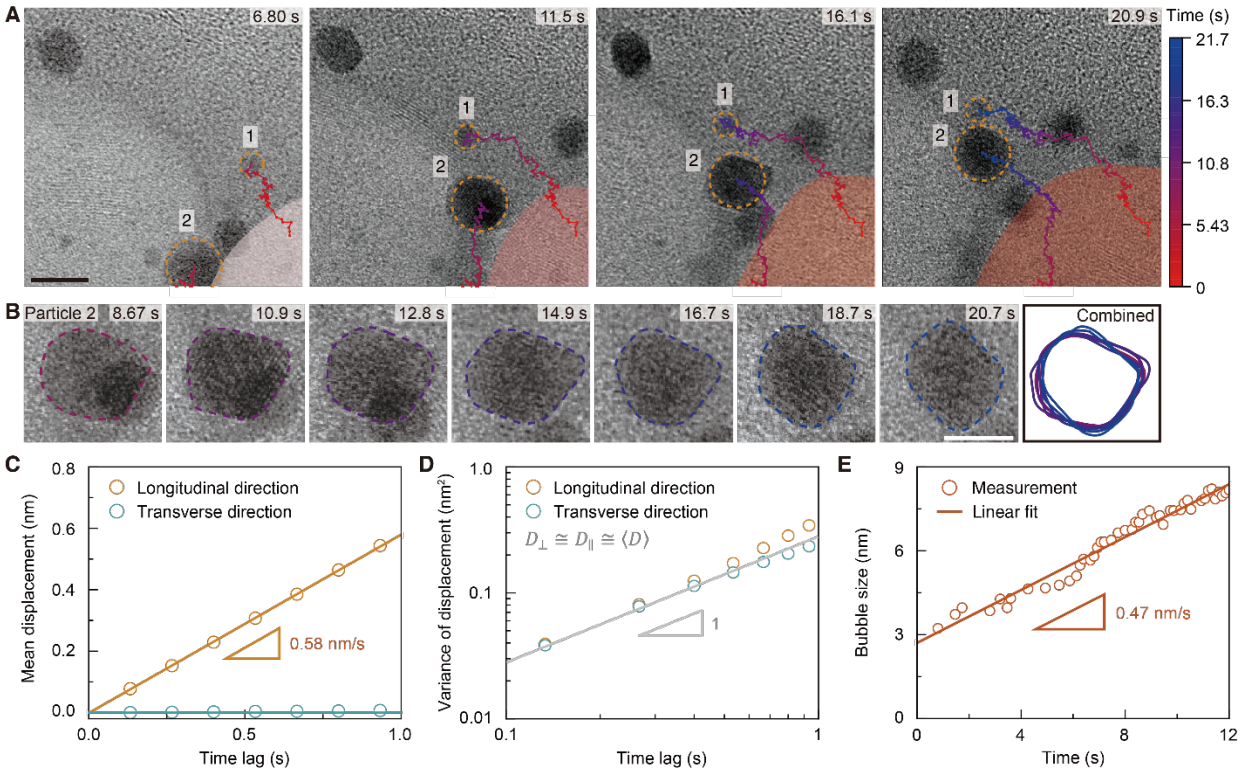

Fig. S25. Effect of liquid-vapor interface movement on nanoparticle motion. (**A**) Time-series TEM images showing the growth of a nanobubble at the right-bottom side of the images (marked with red), and representative trajectories of nanoparticles whose movements are influenced by the growing nanobubble (see also section S6 and movie S5). Scale bar, 5 nm. (**B**) Time-series TEM images of faceted nanoparticles (particle 2 in (A)), showing hindered rotational motion of the nanoparticle pinned at the liquid-vapor interface. Scale bar, 2 nm. (**C**) Mean displacements of the nanoparticles near nanobubble in the direction parallel to the final displacement of each nanoparticle (longitudinal direction, orange circles) and in the direction normal to the final displacement of each nanoparticle (transverse direction, blue circles). (orange line) Linear fit of mean longitudinal nanoparticle displacement, yielding a mean nanoparticle velocity of 0.58 nm/s. (blue line) Linear fit of mean transverse nanoparticle displacement, indicating negligible net nanoparticle movement in the transverse direction. (**D**) Variance of nanoparticle displacements in

longitudinal direction (orange symbols), and transverse direction (blue symbols). (solid line) $4\langle D\rangle t$ with $\langle D\rangle$ indicating the mean diffusion coefficient obtained in Fig. 2A in the main text. (**E**) Nanobubble growth. (symbols) Experimental data. (line) Linear fit, yielding nanobubble growth rate of 0.47 nm/s. The value is comparable to the mean longitudinal nanoparticle velocity obtained in (C).

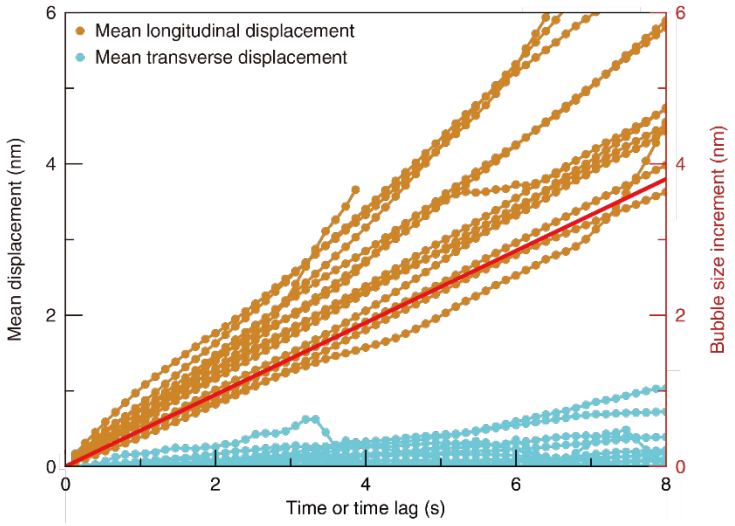

Fig. S26. Displacements of individual nanoparticles near nanobubble. Time-averaged mean displacements of the nanoparticles near nanobubble in their longitudinal directions (orange symbols) and in their transverse directions (blue symbols). See Fig. S25 for the definitions of the longitudinal and transverse directions. (red line) Linear fit of the experimental data for nanobubble size growth. This fit is given in Fig. S25E and reproduced here for comparison.

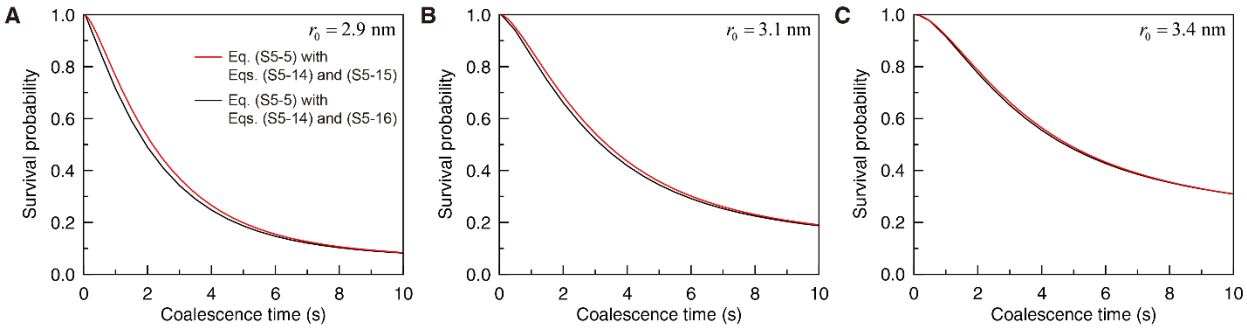

Fig. S27. Comparison between two different theoretical predictions for two-step coalescence kinetics. (**A** to **C**) Survival probabilities as a function of time taken for a pair of nanoparticles initially distant by r_0 to complete coalescence via the formation of transient complexes. Values of r_0 in (**A**), (**B**), and (**C**) are 2.9 nm, 3.1 nm, and 3.4 nm, respectively. The formation of a transient complex between a pair of nanoparticles occurs upon first contact at the center-to-center separation, σ, whose value is given by the sum of the average, 1.35 nm, of particle diameters over all coalescing nanoparticles and the thickness, 1.4 nm, of the double ligand layer. (red line) Theoretical prediction for a pair of nanoparticles following our random walk model in a dynamically heterogeneous environment [Eq. (S4-5) with Eqs. (S4-14) and (S4-15)]. (black line) Theoretical prediction for a pair of nanoparticles undergoing diffusive motion in a dynamically heterogeneous environment [Eq. (S4-5) with Eqs. (S4-14) and (S4-16)]. Eq. (S4-16) is given by the diffusion approximation of Eq. (S4-15) (see section S4). The difference between both theoretical predictions diminishes as r_0 increases. This is because a nanoparticle pair initially distant by larger r_0 should travel a distance much longer than the jump length scale before they can touch.

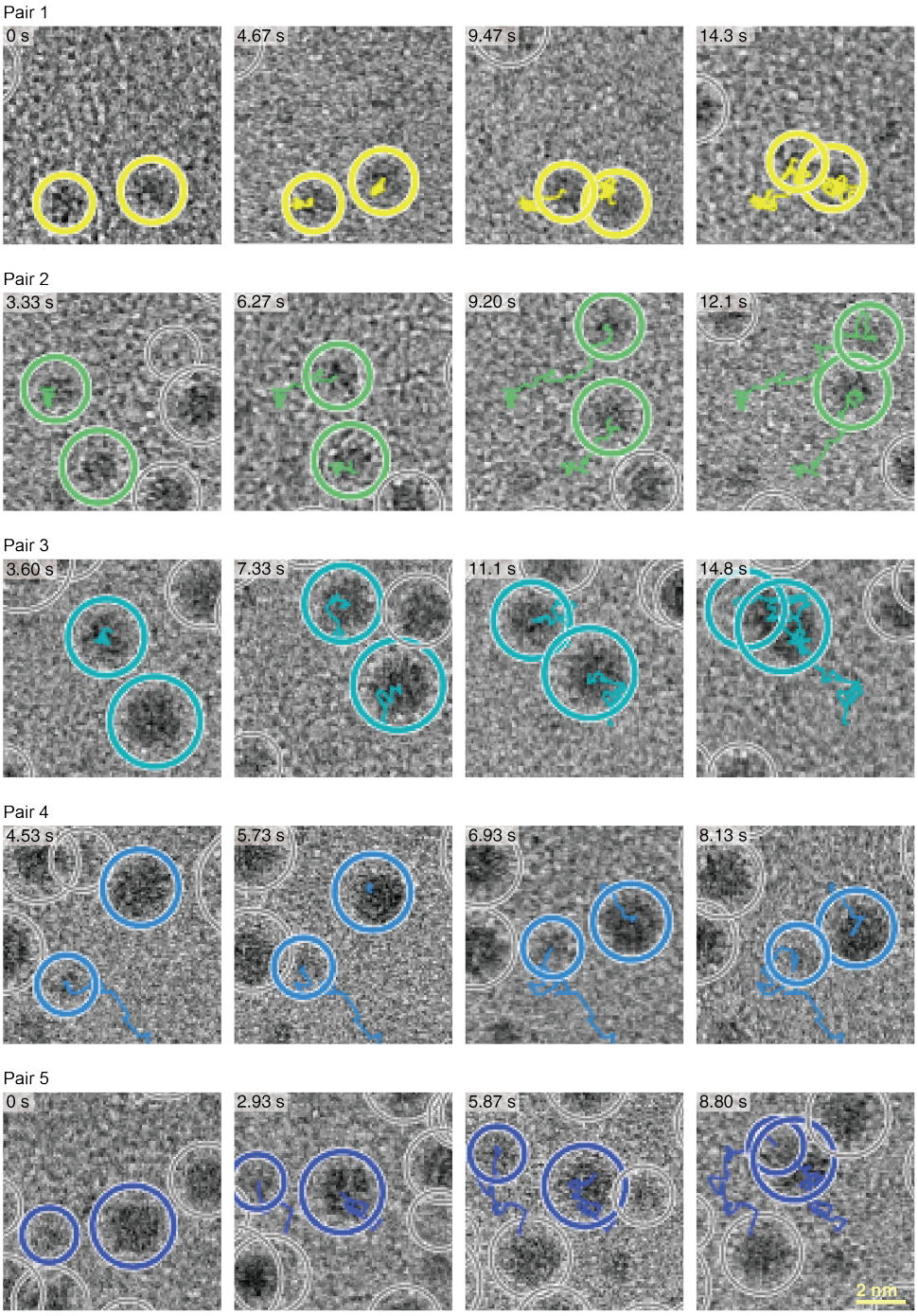

Fig. S28. Time-series TEM images of the nanoparticles forming encounter complexes. (lines) Trajectories of the nanoparticles which are supposed to form an encounter complex. (colored circles) Circle with a radius being the same as the sum of the nanoparticle radius and the ligand length, 0.7 nm, centered on the nanoparticle which is supposed to form an encounter complex.

(grey circles) Circle with a radius being the same as the sum of the nanoparticle radius and the ligand length, 0.7 nm, centered on the nanoparticle which is supposed not to form an encounter complex. Weak overlaps between the grey circles and the colored circles for short time indicate that the encounter pair dynamics is little perturbed by the other nanoparticles near the encounter pair.

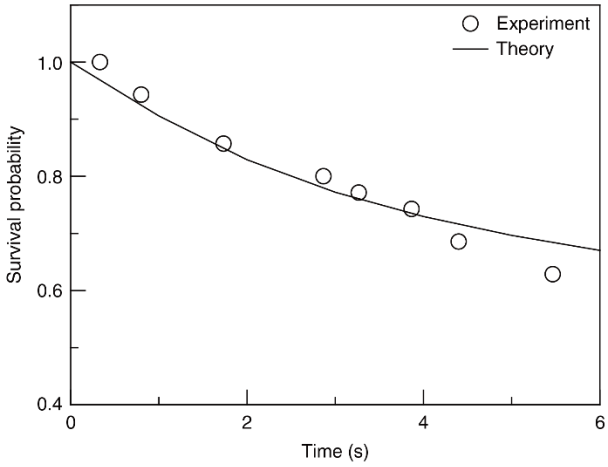

Fig. S29. Survival probability of nanoparticles accounting for nanoparticle coalescence. (symbols) Experimental result for the survival probability of nanoparticles accounting for nanoparticle coalescence. This quantity is calculated as the ratio between the numbers of nanoparticles at a time t and the initial time zero. Here, nanoparticles moving in and out of the field of view are not counted. (lines) Corresponding theoretical result calculated with Eq. (S4-22) and an estimate, 0.007 nm^{-2}, for the initial nanoparticle density. With the mean diffusion coefficient, $\langle D \rangle = 0.12\,nm^2 \cdot s^{-1}$, given in Fig. 2A at hand, the distance a nanoparticle travels for $t = 6$ seconds along the viewing direction can be estimated as $(\langle D \rangle t)^{1/2} = 0.85\,nm$, which is less than the effective contact separation, 2.8 nm, between ligand-passivated nanoparticles, i.e., the sum of the mean nanoparticle diameter, 1.4 nm, and the thickness, 1.4 nm, of the double ligand layer formed upon nanoparticle contact. This means that nanoparticles undergoing coalescence at short times should be initially located at similar distances from the graphene surface, validating a use of the theoretical survival probability calculated in the two-dimensional space (see section S4). In this case, the initial number density for the nanoparticles located at similar vertical distances is supposed to be less than that, 0.03 nm^{-2}, for all nanoparticles observed within the field of view.

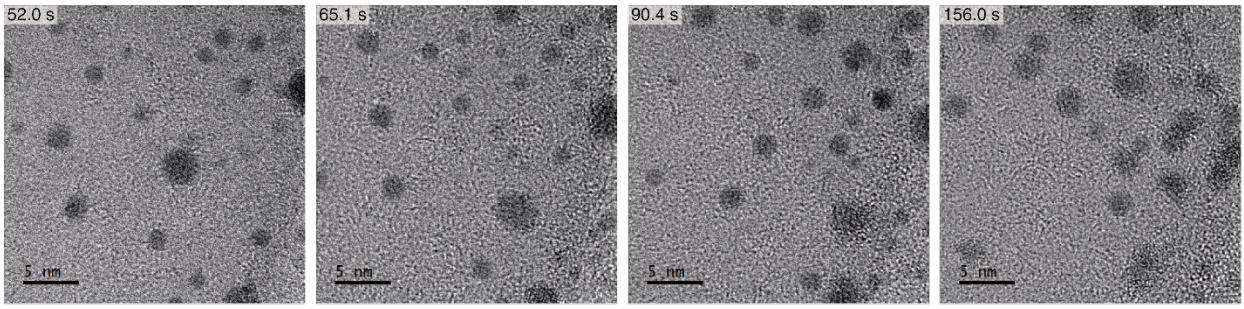

Fig. S30. Nanoparticle dynamics during prolonged electron-beam irradiation. During the prolonged observation of the graphene liquid cell, the motion and spatial arrangement of nanoparticles become different from those described in Fig. 1 (see also movie S6). The time interval between the end of movie S1 and the start of movie S6 is 34 seconds.

Movie S1. Drift-corrected TEM movie of nanoparticle diffusion in quiescent liquid cell

Movie S2. TEM movie of diffusion of oleylamine-passivated Pt nanoparticles in liquid cell

Movie S3. TEM movie showing nanoparticle motion within graphene scroll

Movie S4. TEM movie of a rotating nanoparticle in liquid cell

Movie S5. Drift-corrected TEM movie of nanoparticle diffusion in liquid cell with nanobubble

Movie S6. TEM movie of nanoparticle dynamics in liquid cell after prolonged electron beam irradiation